



HAL
open science

Broadly potent anti-SARS-CoV-2 antibody shares 93% of epitope with ACE2 and provides full protection in monkeys

Craig Fenwick, Priscilla Turelli, Yoan Duhoo, Kelvin Lau, Cécile Herate, Romain Marlin, Myriam Lamrayah, Jérémy Campos, Line Esteves-Leuenberger, Alex Farina, et al.

► To cite this version:

Craig Fenwick, Priscilla Turelli, Yoan Duhoo, Kelvin Lau, Cécile Herate, et al.. Broadly potent anti-SARS-CoV-2 antibody shares 93% of epitope with ACE2 and provides full protection in monkeys. *Journal of Infection*, 2023, 87 (6), pp.524-537. 10.1016/j.jinf.2023.10.008 . hal-04411315

HAL Id: hal-04411315

<https://hal.u-pec.fr/hal-04411315v1>

Submitted on 23 Jan 2024

HAL is a multi-disciplinary open access archive for the deposit and dissemination of scientific research documents, whether they are published or not. The documents may come from teaching and research institutions in France or abroad, or from public or private research centers.

L'archive ouverte pluridisciplinaire **HAL**, est destinée au dépôt et à la diffusion de documents scientifiques de niveau recherche, publiés ou non, émanant des établissements d'enseignement et de recherche français ou étrangers, des laboratoires publics ou privés.

1 *Title:* Broadly potent anti-SARS-CoV-2 antibody shares 93% of epitope with ACE2 and
2 provides full protection in monkeys

3 *Running title:* Potent antibody protects from XBB.1.5 infection in NHPs

4 Craig Fenwick,^{a,†} Priscilla Turelli,^{b,†} Yoan Duhoo,^{c,‡} Kelvin Lau,^{b,‡} Cécile Herate,^{d,‡} Romain Marlin,^{d,‡}
5 Myriam Lamrayah,^{b,‡} Jérémy Campos,^a Line Esteves-Leuenberger,^a Alex Farina,^a Charlène Raclot,^b
6 Vanessa Genet,^b Flurin Fiscalini,^a Julien Cesborn,^a Laurent Perez,^a Nathalie Dereuddre-Bosquet,^d
7 Vanessa Contreras,^d Kyllian Lheureux,^d Francis Relouzat,^d Rana Abdelnabi,^e Pieter Leyssen,^e Yves
8 Lévy,^{f,g,h} Florence Pojer,^b Roger Le Grand,^d Didier Trono,^{b,*} Giuseppe Pantaleo,^{a,i,*}

9

- 10 a- Service of Immunology and Allergy, Department of Medicine, Lausanne University Hospital
11 and University of Lausanne, Lausanne, Switzerland
12 b- School of Life Sciences, Ecole Polytechnique Fédérale de Lausanne, Lausanne, Switzerland.
13 c- School of Basic Sciences, Ecole Polytechnique Fédérale de Lausanne and Faculty of Biology
14 and Medicine, UNIL, Lausanne, Switzerland.
15 d- CEA, Université Paris Sud 11, INSERM U1184, Center for Immunology of Viral Infections and
16 Autoimmune Diseases, IDMIT Department, IBFJ, Fontenay-aux-Roses, France.
17 e- KU Leuven Department of Microbiology, Immunology and Transplantation, Rega Institute for
18 Medical Research, Laboratory of Virology and Chemotherapy, B-3000 Leuven, Belgium.
19 f- VRI, Université Paris-Est Créteil, Faculté de Médecine, INSERM U955, 94010 Créteil, France.
20 g- Inserm U955, Equipe 16, Créteil, France.
21 h- AP-HP, Hôpital Henri-Mondor Albert-Chenevier, Service d'Immunologie Clinique et Maladies
22 Infectieuses, Créteil, France.
23 i- Swiss Vaccine Research Institute, Lausanne University Hospital and University of Lausanne,
24 Switzerland.
25

26 *Key words:* SARS-CoV-2, neutralizing antibodies, Variants of concern, Omicron, ACE2 mimetic

27 *Highlights:*

- 28 • Anti-SARS-CoV-2 neutralizing antibody with ACE2 mimetic binding properties
29 • Broad-spectrum activity against all past and current SARS-CoV-2 variants of concern
30 • Mutations escaping mAb activity bind ACE2 poorly and are rare in circulating virus
31 • Sterilizing protection from XBB.1.5 infection in an NHP challenge model
32

33 †These authors contributed equally and ‡ authors contributed equally.

34 *Lead and co-corresponding authors: Prof. Giuseppe Pantaleo
35 Service of Immunology and Allergy
36 Lausanne University Hospital
37 1011 Lausanne, Switzerland
38 giuseppe.pantaleo@chuv.ch

39 Prof. Didier Trono
40 School of Life Sciences
41 Ecole Polytechnique Fédérale de Lausanne
42 Lausanne, Switzerland
43 didier.trono@epfl.ch
44

45

46 **Abstract**

47 *Objectives:* Due to the rapid evolution of SARS-CoV-2 to variants with reduced sensitivity to
48 vaccine-induced humoral immunity and the near complete loss of protective efficacy of licensed
49 therapeutic monoclonal antibodies, we isolated a potent, broad-spectrum neutralizing antibody
50 that could potentially provide prophylactic protection to immunocompromised patient
51 populations.

52 *Methods:* Spike-specific B-cell clones isolated from a vaccinated post-infected donor were
53 profiled for those producing potent neutralizing antibodies against a panel of SARS-CoV-2
54 variants. The P4J15 antibody was further characterized to define the structural binding epitope,
55 viral resistance and *in vivo* efficacy.

56 *Results:* The P4J15 mAb shows <20 ng/ml neutralizing activity against all variants including
57 the latest XBB.2.3 and EG.1 sub-lineages. Structural studies of P4J15 in complex with Omicron
58 XBB.1 Spike show that the P4J15 epitope shares ~93% of its buried surface area with the ACE2
59 contact region, consistent with an ACE2 mimetic antibody. *In vitro* selection of SARS-CoV-2
60 mutants escaping P4J15 neutralization showed reduced infectivity, poor ACE2 binding, and
61 mutations are rare in public sequence databases. Using a SARS-CoV-2 XBB.1.5 monkey
62 challenge model, P4J15-LS confers complete prophylactic protection with an exceptionally
63 long *in vivo* half-life of 43 days.

64 *Conclusions:* The P4J15 mAb has potential as a broad-spectrum anti-SARS-CoV-2 drug for
65 prophylactic protection of at-risk patient populations.

66

67 **MAIN**

68 The SARS-CoV-2 virus which lead to the global COVID-19 pandemic is responsible for >767
69 million confirmed infections and almost 7 million fatalities worldwide (WHO Coronavirus
70 (COVID-19) Dashboard <https://covid19.who.int/>) (1). Enormous efforts by the scientific and
71 medical communities in vaccine, antiviral drugs and monoclonal antibody development have
72 allowed most people to return to normal lives after the peak of the pandemic, typified in most
73 parts of the world by lockdowns, isolation, and overwhelmed health care networks. However,
74 these hard-fought victories are being eroded by the continued regional and international spread
75 of variants of concern (VOC), which are both more transmissible and more resistant to immune
76 responses (2-4). SARS-CoV-2 infection leading to COVID-19 disease is of increased concern

77 due to the rapidly waning immunity in the general population, the apathy that has developed
78 for receiving vaccine boosts and the reduced levels of neutralizing antibodies generated by even
79 the most recent bivalent vaccines (which include the ancestral SAR-CoV-2 and Omicron BA.1
80 or BA.4/5 Spike) against current VOCs (5). Alarming, these factors contribute to SARS-CoV-
81 2 infection being a leading cause of death in children and adolescents up to 19 years of age,
82 accounting for 2% of all deaths in this age group in the year prior to August 2022 (6). The
83 greatest unmet medical need is the >30 million immunocompromised individual in the US and
84 Europe alone that are at high risk of infection due to their inability to mount a protective
85 humoral immune response following vaccination (7, 8). These at-risk individuals include
86 people with blood and immune cell cancers, transplantation patients and recipients of
87 immunosuppressive drugs, all of which account for >40% of hospitalizations with breakthrough
88 SARS-CoV-2 infections (9, 10). Since the emergence of the BQ.1, BQ.1.1 and XBB.1 lineages
89 in the fall of 2022, all authorized therapeutic mAbs have become almost completely ineffective,
90 including Evusheld, the combination of tixagevimab (AZD8895) and cilgavimab (AZD1061)
91 mAbs that was designed for therapeutic and prophylactic purposes (11). Although there are
92 recent reports in the literature identifying mAbs with some breadth of neutralizing activity, most
93 are significantly less potent against the circulating variants than antibodies that previously
94 demonstrated protection in the clinic (12-15). Furthermore, the SARS-CoV-2 virus will
95 continue to evolve due to both the tremendous pool of circulating viruses and selective pressures
96 exerted by immune responses present in the general population, necessitating that new mAbs
97 be developed to counter currently circulating variants and anticipate future adaptations. Here
98 we report the isolation of the human mAb, P4J15, that binds the Spike receptor binding domain
99 (RBD) and through blocking ACE2 receptor binding, exerts a potent neutralizing activity
100 against all current SARS-CoV-2 variants. Structural studies reveal that this broad activity can
101 be attributed to the high binding surface area of the P4J15 epitope, which includes residues
102 essential for efficient ACE2 binding and infection. Live virus resistance studies confirmed that
103 P4J15 escape mutants selected in cell culture were poorly infectious, owing to RBD mutations
104 strongly reducing affinity for the ACE2 receptor. Accordingly, the corresponding escape
105 mutations were found only at low frequency in the GISAID sequence database, confirming their
106 detrimental effect on virus fitness. Finally, P4J15 conferred near complete protection from
107 infection in hamster and monkey live virus challenge studies performed with Omicron BA.5
108 and XBB.1.5 variants, respectively. With this demonstrated *in vivo* efficacy against the most
109 recent variants, neutralizing potency and breadth of protection, we propose that P4J15 could be
110 a strong candidate for clinical development.

111 **RESULTS**

112 **P4J15 is a potent and broadly neutralizing anti-SARS-CoV-2 monoclonal antibody**

113 As part of a longitudinal study to monitor the waning humoral immune response in a cohort of
114 20 donors, we performed routine serum testing of anti-Spike and anti-Nucleocapsid antibodies.
115 One donor with weak neutralizing antibody levels consistent with prior SARS-CoV-2 infection,
116 received two doses of the mRNA-1273 vaccine in late 2021 and became SARS-CoV-2 positive
117 four weeks later during the Omicron BA.1 wave. Two months later, this donor had among the
118 highest serum antibody levels in all donors tested, with excellent breadth of neutralization
119 against Omicron BA.1 and a panel of other pre- and post- Omicron SARS-CoV-2 variants in a
120 trimeric Spike-ACE2 surrogate neutralization assay (16). To focus our mAb screening efforts,
121 we sorted Omicron BA.1 Spike-binding memory B cells and identified a panel of 16 Spike
122 binding antibodies by profiling antibody supernatants from B cell clones. The P4J15 mAb,
123 produced by expression of paired heavy and light chains in ExpiCHO cells, showed the highest
124 affinity for the SARS-CoV-2 ancestral, Alpha, Beta, Gamma, Delta, Omicron BA.1, BA.1.1,
125 BA.2, BA.2.75.2, BQ.1, BQ.1.1, XBB.1 and the RaTG13 sarbecovirus Spike trimer proteins,
126 while showing only low levels of binding to SARS-CoV-1 Spike (**Supplementary Data Fig.**
127 **1a-b**). Profiling studies in a Luminex Spike binding assay showed that the purified P4J15 mAbs
128 bound SARS-CoV-2 Spike proteins in our panel with IC₅₀ values ranging from 0.6 to 1.5 ng/ml
129 (**Supplementary Data Fig. 1b**) and RaTG13 Spike with an IC₅₀ of 11 ng/ml. Using our Spike-
130 ACE2 surrogate neutralization assay, we also found that P4J15 had the most potent and broadest
131 activity in blocking ACE2-binding to Spike trimers from our extensive panel of SARS-CoV-2
132 variants, with IC₅₀ values below 5 ng/ml (**Supplementary Data Fig. 2a-b**). These studies
133 indicate that P4J15 has a superior affinity in binding and Spike-ACE2 blocking profile
134 compared to a panel of approved or clinically advanced anti-SARS-CoV-2 mAbs including
135 AZD8895 and AZD1061 from AstraZeneca (17), ADG-2 from Adagio (18), bebtelovimab from
136 Eli Lilly (19) and S309/sotrovimab from Vir/GSK(20).

137 Cross-competitive Spike trimer binding studies performed with our panel of comparator anti-
138 SARS-CoV-2 mAbs and P2G3/P5C3 mAbs previously described by our group (21, 22)
139 revealed that P4J15 binds an overlapping epitope with AZD8895 and P5C3 class 1 mAbs,
140 although neither of these mAbs identified early in the pandemic significantly binds to post-
141 BA.4/5 Omicron variants. No cross-competitive binding was observed between P4J15 and the
142 class 3 mAbs sotrovimab, bebtelovimab and P2G3, whereas the class 4 mAb ADG-2 showed

143 mixed competition results with P4J15, depending on which antibody was bound to Spike first.
144 **(Supplementary Data Fig. 3).**

145 **P4J15 outperforms clinically relevant antibodies in pseudovirus-based neutralization** 146 **assays**

147 We next evaluated the activity of P4J15 compared with a panel of clinically approved mAbs in
148 pseudotyped lentiviral and SARS-CoV-2 virus-like particle (VLP) cell-based neutralization
149 assays. P4J15 demonstrated potent neutralizing activity against lentiviruses pseudotyped with
150 Spike from the ancestral 2019-nCoV (D614G), Alpha, Beta, Delta, Omicron BA.1, BA.4/5 and
151 BA.2.75.2 VOCs with EC₅₀ values of 41, 14, 19, 16, 9, 5 and 9 ng/ml, respectively (**Fig. 1a-b**).
152 In contrast to all other reference antibodies, P4J15 strongly neutralized the Omicron BQ.1,
153 BQ.1.1, XBB.1 Spike pseudoviruses with an EC₅₀ values of 6, 9 and 14 ng/ml, respectively
154 (**Fig. 1b-c**) and showed no significant loss of activity as compared to the other VOCs. In parallel
155 testing, P4J15 was 13- to 300-fold more potent than sotrovimab, while the Evusheld dual
156 combination of neutralizing mAbs, and bebtelovimab were almost inactive against BQ.1.1 and
157 XBB.1 VOCs with EC_{50s} >8700 ng/ml. As Spike is incorporated at the plasma membrane in
158 pseudotyped lentivectors and in the ER-Golgi intermediate compartment (ERGIC) in SARS-
159 CoV-2 viruses, we decided to use a SARS-CoV-2-based particle (VLPs) as a second system to
160 profile P4J15 efficacy. These VLP-based assays confirmed results obtained in the lentiviral
161 assay pseudotyped with Spike from Delta BA.1, BA.4/5, BA.2.75.2, BQ.1, BQ.1.1 and XBB.1
162 (EC₅₀ values of 15, 2, 4, 10, 10, 13 and 13 ng/ml, respectively) (**Fig. 1b** and **1d**). VLP
163 neutralizing assays also revealed that P4J15 retained full neutralizing activity against the latest
164 circulating Omicron sub-lineages XBB.1.5, CH.1.1, XBB.1.16, XBB.1.16.1, XBB.2.3 and
165 EG.1 with EC₅₀ values of 6, 10, 9, 13 18, and 16 ng/ml (**Fig. 1e** with results summarized in **Fig.**
166 **1b**).

167

168 **Cryo-electron microscopy structure of P4J15 Fab in complex with the Spike trimer**

169 To understand the structural basis of P4J15 potent neutralization of SARS-CoV-2 variants of
170 concern, the complex formed by Omicron XBB.1 SARS-CoV-2 Spike trimer and P4J15 Fab
171 fragments was characterized using single particle cryo-electron microscopy (cryo-EM). The
172 single particle cryo-EM reconstruction of the Omicron XBB.1 Spike trimeric ectodomain
173 bound to the Fab at a 3.01 Å resolution and the P4J15 Fab binding RBD in the up- or open-
174 conformation (**Fig. 2a** and **Supplementary data Fig. 4a-e** and **6**). P4J15 binds RBD with a

175 buried surface area of approximately 828 Å² as a Class 1 neutralizing mAb, recognizing an
176 epitope on the SARS-CoV-2 RBD that largely overlaps with the ACE2 receptor binding motif.
177 To characterize the P4J15 paratope and epitope interface in detail, we performed local
178 refinement of the P4J15 Fab-RBD interacting region and reached a resolution of 3.85 Å with
179 well-defined density, allowing clear interpretation of sidechain positions at the interface. We
180 also used EMReady (23), a deep learning tool, to enhance the quality even further (**Fig. 2b-c**
181 **and Supplementary data Fig. 4-5**). The P4J15 paratope interactions are mediated mainly
182 through electrostatic and hydrophobic contacts and involve 26 residues of the RBD, bound by
183 the three heavy chain CDRs, two light chain CDRs and residues of the heavy chain Frame
184 region 3 (FRH3) of the P4J15 mAb. The CDRH1, CDRH2 and FRH3 loops of P4J15 (**Fig. 2d-**
185 **f and Supplementary data Fig. 7-8**) form contacts with the Gly447-Phe456 and Gly485-
186 His505 saddle-like region of the RBD that encompasses the β5 and β6 antiparallel beta sheet of
187 the ACE2 binding region (**Fig. 2e**). CDRH3 sits upon the RBD Arg454-Lys458 loop and
188 together with the CDRL1 and CDRL3 forms additional contacts with the Tyr473-Lys478 and
189 Ser486-Tyr489 of the ACE2 interface region (**Fig. 2f**). These contact residues are further
190 illustrated in **Figure 2g** with a structural model of the RBD viewed from above and the P4J15
191 contact buried surface on the RBD shaded in dark grey and compared to the ACE2 contact
192 residues. It is important to underscore that 22 of these P4J15 contact residues on the RBD are
193 shared with key contacts formed between the RBD (**Fig. 2g**) and the ACE2 receptor, which is
194 essential for virus binding and infection of target cells. The common area on the RBD for these
195 22 residues that contact P4J15 and ACE2 is on average 774 Å², which is almost 93% of the
196 P4J15 epitope and 87% of the 887 Å² contact area with ACE2. Based on these observations,
197 we propose that P4J15 may act as an ACE2 mimetic antibody and that it will be difficult for
198 the virus to develop resistance mutations that completely disrupt the P4J15-RBD interaction
199 without adversely affecting the ACE2-RBD interaction.

200

201 **P4J15 viral escape mutations have reduced infectivity and ACE2 binding**

202 To gain insight into the predicted clinical value of P4J15 and variant residues in the SARS-
203 CoV-2 Spike that may affect the mAbs neutralizing activity, we characterized the emergence
204 of escape mutants in live virus tissue culture studies. For this, we grew SARS-CoV-2 Omicron
205 BA.2.75.2 and Omicron BQ.1 variants in the presence of sub-optimal neutralizing doses of
206 P4J15 for three passages to generate a heterogeneous viral population, before switching to
207 stringent mAb concentrations in order to select authentic escapees (**Fig. 3a**). Viral genome

208 sequencing of these mAb-resistant mutants pointed to the importance of Spike substitutions
209 F456S, A475D, G476D, N477D/K, N487S/D/K escaping P4J15 in the BA.2.75.2 selection
210 studies and G476D, N487S/T/D/K, Y489H substitutions identified with BQ.1 virus studies
211 (**Fig. 3b**). The identified mutations were then generated by site-directed mutagenesis in a Spike
212 BA.2.75.2 and Spike BQ.1 expression vectors and used to generate mutant Spike virus-like
213 particles (VLPs), allowing us to measure the impact of these mutations on the neutralizing
214 capacity of P4J15 and on viral infectivity. Spike mutations that conferred a near complete loss
215 of neutralizing activity in the BA.2.75.2 VLP assay were F456S, A475D, G476D, N487D,
216 N487K, and N487T while N477D, N477K and N487S conferred a 14- to 29-fold loss of activity
217 (**Fig. 3c**). Similarly, in the BQ.1 Spike VLP assay, G476D, N487D, N487K, and N487T
218 induced resistance to neutralization by P4J15 along with the Y489H mutation, while the N487S
219 mutation conferred only partial resistance (**Fig. 3c**). However, the infectivity of select VLPs
220 was reduced with Spike proteins harbouring many of the escapee mutations (**Fig. 3d**) including
221 A475D and N487D in the BA.2.75.2 Spike and N487D, N487K and N487T in BQ.1 Spike.
222 Furthermore, using the ACE2-RBD interactive tool developed by Jesse Bloom's lab(24), it was
223 found that all the Spike escape mutations in RBD induced a strong, 1- to 3-log reduction in
224 binding affinity for ACE2 relative to the Omicron BA.2 Spike reference strain (**Fig. 3e**). The
225 reduced binding affinity of ACE2 for the Spike RBD escape mutations was expected based on
226 our structural data in **Figure 2e-g**, as these residues are important for both P4J15 and ACE2
227 binding to the RBD. Furthermore, we examined the GISAID EpiCoV database to determine the
228 frequency of the Spike mutations mediating escape to P4J15 neutralization. They were all found
229 to be extremely rare and present in less than 0.0051% of the >15'6 million sequences deposited
230 as of June 2023 (**Fig 3c**). Therefore, escape mutations to P4J15 are only present at very low
231 frequency in viruses isolated from infected individuals, consistent with the marked reduction in
232 infectivity and/or ACE2 binding measured *in vitro* for the corresponding viruses and Spike
233 proteins (**Fig. 3d-e**). Finally, to confirm the barrier to P4J15 viral resistance imposed by the
234 obligatory Spike-ACE2 interaction, we bioinformatically identified the rare but most common
235 amino acid substitutions at positions identified at the P4J15-RBD contact site and in our
236 resistance studies. As shown in **Figure 3f**, with substitutions made to the Omicron BA.5 or
237 BQ.1 Spike, none of the mutations tested, including N417D, V445D, G446D, N450D, L455F,
238 F456L, K458H, S459P, A475V, G476S, N477G, T478R, G485D, P491S, S494P and G504D
239 that are within or adjacent to the P4J15-RBD contact site, significantly reduced the neutralizing
240 potency of P4J15. These studies support the hypothesis that the large, buried surface area bound

241 by P4J15 translates into the antibody's ability to lose some of these contacts without affecting
242 the overall binding and neutralizing properties.

243

244 **Prophylactic use of P4J15 in the hamster Omicron BA.5 infection model**

245 To further validate the potency of P4J15, *in vivo* live virus challenge experiments were
246 performed in a prophylactic hamster challenge model of SARS-CoV-2 infection. Animals were
247 dosed with 5, 1 or 0.5 mg/kg of P4J15, 5 mg/kg of bebtelovimab or a human IgG1 control,
248 challenged two days later with an intranasal inoculation of the Omicron BA.5 SARS-CoV-2
249 virus (**Fig. 4a**) and lung tissue from the hamsters were examined four days later for infectious
250 virus and viral RNA. Infectious virus was undetectable in the lungs of all but one P4J15 treated
251 hamsters in the lowest dose 0.5 mg/kg group, which still had a >2-log reduction in levels of
252 infectious virus compared to the isotype mAb-treated control animals (**Fig. 4b**). In comparison,
253 1 out of 5 hamsters in the 5 mg/kg bebtelovimab group had detectable levels of infectious virus.
254 Importantly, protective plasma levels of P4J15 in Omicron BA.5 challenged hamsters were
255 shown to be ~7 µg/ml, whereas in the bebtelovimab arm of the study, the one treated animal
256 with detectable infection virus in the lungs had mAb plasma levels of 83 µg/ml. Interestingly,
257 although all P4J15 treatment groups showed a significant reduction in genomic RNA levels,
258 relatively high levels were detected in two and three hamsters for the 1 and 0.5 mg/kg dose
259 arms (**Fig. 4c**). This indicates that although P4J15 treatments virtually eliminated infectious
260 virus, RNA, presumably from inactivated virus, was still detectable in select animals four days
261 after challenge.

262

263 **P4J15 shows full prophylactic therapeutic efficacy in cynomolgus macaques**

264 We next evaluated P4J15 LS with M428L/N434S half-life extension mutations in the Fc
265 domain in mediating protection from live SARS-CoV-2 Omicron XBB.1.5 virus infection in a
266 pre-exposure challenge study in cynomolgus macaques. Non-human primates (NHP, n=6) were
267 administered 5 mg/kg of P4J15 intravenously and challenged 72 hours later with 1×10^5 TCID₅₀
268 of SARS-CoV-2 Omicron XBB.1.5 virus via a combined intranasal and intratracheal route (**Fig.**
269 **5a**). Following viral challenge, control animals (n=4, tested in parallel and n=2 historical
270 controls) showed similar genomic (g)RNA levels and kinetics with median peak viral loads
271 (VL) of 7.3, 7.1 and 6.4-log₁₀ copies/ml gRNA in nasopharyngeal swabs, tracheal swabs and
272 bronchoalveolar lavage (BAL) samples, respectively, at 2-3 days post challenge (**Fig. 5b-d**).

273 In comparison, the six P4J15 LS treated NHPs had essentially undetectable levels of gRNA at
274 all sample and time points tested. This complete protection provided by P4J15 LS was further
275 confirmed by evaluating signs of active viral replication, as assessed by subgenomic (sg)RNA
276 levels, which peaked in control animals at 3-4 days post-challenge with nasopharyngeal swabs,
277 tracheal swabs and BAL showing median values of 5.2- 5.2 and 4.2-log₁₀ copies per ml,
278 respectively (**Fig. 5e-g**). As expected with the almost complete viral suppression, area under
279 the curve analysis (AUC) for P4J15 LS treated NHPs showed a significant reduction in gRNA
280 compared to controls in nasopharyngeal samples collected from left and right nostrils
281 throughout the study and tracheal samples ($P < 0.0001$ and 0.0022 , respectively) (**Fig. 5h**).
282 Similar significantly reduced levels of sgRNA in the AUC analysis was observed in P4J15 LS
283 treated NHPs where sgRNA was undetected in all samples analysed throughout the study period
284 (**Fig. 5i**). This indicates the absence of any replicating virus and the complete prophylactic
285 protection provided by P4J15 LS in a non-human primate model. Finally, pharmacokinetic
286 analysis of the NHPs dosed with P4J15 LS showed a long *in vivo* half-life of 43 days and a
287 mean serum concentration of 75 µg/ml in the six animals 46 days after dosing (**Fig. 5j**). In
288 comparison, the Evusheld antibodies AZD1061 and AZD8895 with the YTE extended half-life
289 mutations showed an NHP *in vivo* half-life of 19 days (25).

290 **DISCUSSION**

291 As the WHO declares that the emergency phase of the SARS-CoV-2 pandemic has ended, the
292 strain on the health care system continues with hospitalization rates from new infections still
293 reaching >15'000 patients per week across North America and Europe (Supplementary Table
294 1). Furthermore, it was recently reported that 10% of individuals suffer from long COVID after
295 Omicron infection, with clinical symptoms that can include fatigue, brain fog, and dizziness
296 lasting for upwards of six months (26). Newly emerged SARS-CoV-2 variants, including
297 BQ.1.1 and XBB variants, now up to XBB.2.3, are increasingly infectious and immune evasive,
298 significantly eroding the protection conferred by vaccines and previous infections. In addition,
299 almost all licensed monoclonal antibodies for SARS-CoV-2 are inactive against currently
300 circulating VOCs.

301 Here we report the isolation of the fully human P4J15 antibody from a vaccinated, convalescent
302 donor with superior breadth and neutralizing potency to all other reported antibodies against
303 SARS-CoV-2 VOCs up to the most recent XBB.2.3 (12-15). This unique antibody has been
304 extensively optimized *in vivo* by somatic hypermutation, as evidenced by the low 82.5% and
305 90.5% identity of the P4J15 heavy and light chain sequences, respectively, relative to the

306 IGHV4-34*01 and IGKV1-33*01 germline genes. The uniqueness of P4J15 is also illustrated
307 by the low identity of 53.3% with the closest match of the 12016 anti-spike HCDR3 sequences
308 reported to date.

309 Cryo-EM performed with the antibody Fab bound to Omicron XBB.1 Spike revealed that P4J15
310 binds as a Class 1 mAb to the up-RBD conformation of the Spike trimer with a large, buried
311 surface area of 828 Å². Importantly, of the 26 RBD residues that make up the P4J15 binding
312 epitope, 22 are shared with those used for ACE2 binding, representing 93% of the P4J15 contact
313 site. Conversely, ~87% of the 887 Å² ACE2 binding epitope on RBD is shared by P4J15, which
314 accounts for its potent neutralizing mechanism of action through blockade of ACE2 binding to
315 all SARS-CoV-2 Spike variants tested to date. Interestingly, there are 10 RBD residues shared
316 between P4J15 and ACE2 that have undergone evolutionary fine-tuning to evade neutralizing
317 antibody responses while optimizing ACE2 binding and/or viral infectivity. Through the
318 pandemic, these substitutions relative to the ancestral Spike include S477N, T478K/R,
319 E484K/A, F486V/S/P, F490S, Q493R/Q, G496S, Q498R, N501Y and Y505H. Selection of
320 these mutations over the last 42 months has contributed to the XBB.1 and BQ.1.1 variants
321 exhibiting a 7.6- and 17-fold increase in infectivity relative to Omicron BA.2, respectively, as
322 monitored in pseudovirus and cell fusion assays (27, 28). Indeed, similar to ACE2 and
323 consistent with having ACE2 mimetic properties, we see that P4J15 has improved neutralizing
324 activities against post-Omicron variants (EC₅₀ values of 5 to 14 ng/ml) compared to the
325 ancestral 2019-nCoV (EC₅₀ of 41 ng/ml) in the Spike pseudotyped lentiviral neutralization
326 assays.

327 Even with the highly overlapping binding epitope of P4J15 and ACE2 on the Spike RBD, we
328 confirmed that the development of resistance is inevitable when a virus is under selective
329 pressure, at least *in vitro*. Mutations centred at F456, A475, G476, N477, N487 and Y489 did
330 confer escape to neutralization by P4J15 but also reduced binding to ACE2 by 1- to 3-logs,
331 indicating that the virus incurs a significant fitness penalty in developing resistance. Although
332 epistasis is always possible to complement for deleterious mutations (29), the almost complete
333 absence of these specific resistance mutations within the GISAID database confirms that the
334 virus cannot easily escape the type of inhibition imposed by P4J15 without compromising its
335 ability to spread in the population. Of note, substitutions at some of the incriminated positions
336 are detectable in public sequence databases, albeit at very low frequency, but these mutations
337 do not confer resistance to neutralization by P4J15, which requires very specific amino acid
338 substitutions. We note that in select Spike mutations, there are discrepancies between the

339 infectivity data obtained in the VLP-based assay and the predicted binding affinity of the
340 resistant Spike for the ACE2 receptor, illustrating the limitations of any *in vitro* assay. The
341 relative ACE2 binding data were obtained from Jesse D. Bloom's online interactive tool. While
342 this deep mutational scanning approach is a highly valuable and well controlled approach for
343 predicting the potential effects of mutations in the RBD, it has shortcomings, as acknowledged
344 by its inventors themselves. These include i) differences in glycan structures on the Spike
345 surface in yeast vs. human cells, ii) use of only the RBD portion of the Spike protein to assess
346 the impact of mutations, iii) assessment of the effects of mutations in the BA.2 background, and
347 iv) information limited to the affinity of the tested Spike protein for its ACE2 receptor, without
348 consideration of any other step important for viral entry, let alone genome
349 replication/expression. The infectivity measurements were performed with of HEK 293T cell
350 produced VLPs as tested in HEK 293T ACE2/TMPRSS2 target cells. The results indeed
351 indicate that some of the escape mutants, in the VLP assay, are slightly more infectious than
352 the wild-type control whereas the said mutations alter ACE2 recognition when tested in yeast
353 with an RBD-only construct. While on the one hand, the VLP assay is predicted to reflect more
354 fully the multiple steps leading to the delivery of the viral genetic content into its target cells,
355 on the other hand, the rarity of these mutations in nature tells us that this system still misses
356 features important for viral fitness. Part of this difference may be virological, including the
357 concentration of receptor and entry accessory mediators on HEK 293T cells overexpressing
358 ACE2 and TMPRSS2, which cannot be expected to mimic that found on the respiratory
359 epithelium, and the stoichiometry of Spike on VLPs and SARS-CoV-2 virions, which is not
360 identical, and other differences are immunological, including the sensitivity to the prevailing
361 immunity in the population.

362 Finally, *in vivo* efficacy studies performed with two animal models demonstrate that P4J15
363 provides exceptional levels of protection against infection. In hamsters challenged with the
364 Omicron BA.5 virus, animals pre-dosed with 0.5 mg/kg of mAb resulting in serum
365 concentrations as low as 7 µg/ml were strongly protected from infection with almost complete
366 suppression of infectious virus in the lungs. A cynomolgus monkey challenge performed with
367 the latest available XBB.1.5 SARS-CoV-2 variant further revealed that P4J15 at 5 mg/kg
368 produced near sterilizing protection in all six treated animals, with only two positive samples
369 with viral genomic RNA near the detection limit of the RT-PCR assay out of a total of 192
370 nasal, tracheal and BAL samples tested. These results are among the most definitive protection
371 results for SARS-CoV-2 non-human primate challenge studies (25, 30, 31). In addition to

372 complete *in vivo* efficacy, the P4J15 antibody produced with the LS extended half-life
373 mutations in the Fc domain showed an extremely long terminal *in vivo* half-life of 43 days,
374 more than twice that observed for Evusheld in a similar NHP study. Given that Evusheld
375 antibodies achieved an *in vivo* half-life of 90 days in human clinical trials (25), it is expected
376 that P4J15 LS could provide a similar duration of prophylactic protection of more than six
377 months following a single dose of antibody administered by intravenous, intramuscular or
378 intraperitoneal injection (32, 33). With its impressive *in vivo* protection, P4J15 LS could form
379 a strong basis for prophylactic therapy in immunocompromised patients. To supplement this
380 activity and protect against the development of resistance (34), P4J15 could potentially be
381 combined as a cocktail with a second neutralizing antibody that binds a distinct epitope on
382 Spike. For example, although sotrovimab is only weakly to moderately active against some of
383 the newer SARS-CoV-2 variants, this antibody would help to suppress any low-level, poorly
384 fit viral quasi-species that are resistant to P4J15.

385 The world is at a critical juncture in the SARS-CoV-2 pandemic where humoral
386 protection afforded by vaccines is waning, the public at large has become complacent and new
387 variants with ever-increasing infectivity and immune resistance are emerging regularly. As a
388 result of these factors, the most vulnerable in our population, the immunocompromised, those
389 with comorbidities such as cancer and the elderly, who are unable to mount a strong protective
390 humoral immune response after vaccination (7, 35), are at significantly increased risk of
391 hospitalization and death. Given the potent neutralizing activity of P4J15, its ACE2 mimetic
392 properties that may help to limit the development of resistant virus and the impressive complete
393 *in vivo* protection in the non-human primate model, this monoclonal antibody has the potential
394 to be a superior anti-SARS-CoV-2 mAb for prophylactic and/or potentially therapeutic
395 interventions. Furthermore, the breadth of potent neutralizing activity against all current VOCs
396 and variant quasi-species within public SARS-CoV-2 sequence databases suggests that it may
397 be able to neutralize many future VOCs that could emerge in the months and years ahead,
398 providing a sustainable and long-lasting solution to protect the most vulnerable in our
399 population.

400

401 **Materials and methods**

402 **Study COVID-19 donors**

403 Serum and blood mononuclear cell samples were from donors participating in the ImmunoCov
404 and ImmunoVax studies performed by the Immunology and Allergy Service, Lausanne
405 University Hospital with all participants being adults of varying ages and having signed
406 informed consent forms for the use of biological samples. Study design and use of subject
407 samples were approved by the Institutional Review Board of the Lausanne University
408 Hospital and the ‘Commission d’éthique du Canton de Vaud’ (CER-VD with trial reference
409 numbers 2020-00620 and 2021-00041, respectively).

410 **Production of SARS-CoV-2 Spike proteins**

411 SARS-CoV-2 Spike mutations are listed in Supplementary Table 1. Production of 2019-nCoV
412 (D614G), Alpha, Beta, Delta and Omicron BA.1 variants has already been described (21). BA.2
413 and further Omicron sub-lineages ORFs were cloned by 1kb gBlocks assembly (IDT DNA) and
414 In-Fusion cloning into the nCoV-BA.1 plasmid described earlier (36). Single mutations were
415 further introduced by PCR-mediated mutagenesis in each sub-lineage. The full Omicron ORFs
416 were sequence verified for all the clones. The final constructs encode the Spike ectodomains,
417 containing a native signal peptide, the 2P and furin cleavage site mutations, a C-terminal T4
418 foldon fusion domain to stabilize the trimer complex followed by C-terminal 8x His and 2x
419 Strep tags for affinity purification. The trimeric Spike variants were produced and purified as
420 previously described (16). The purity of Omicron Spike trimers used for cryo-EM was
421 determined to be >98% pure by SDS-PAGE analysis. Biotinylation of Spike or RBD proteins
422 was performed using the EZ-Link™ NHS-PEG4-Biotin (Life Technologies, USA) using a 3-
423 fold molar excess of reagent and using the manufacturer’s protocol. Biotinylated proteins were
424 buffer exchanged with PBS using an Amicon Ultra-0.5 with a 3 kDa molecular weight cut-off.
425 Spike and RBD tetramers were prepared fresh before use and formed by combining
426 biotinylated proteins with PE-conjugated Streptavidin (BD Biosciences, USA) at a molar ratio
427 of 4:1.

428 **Binding and ACE2 blocking studies with SARS-CoV-2 Spike**

429 Luminex beads used for the serological and purified antibody binding assays were prepared by
430 covalent coupling of SARS-CoV-2 proteins with MagPlex beads using the manufacturer’s
431 protocol with a Bio-Plex Amine Coupling Kit (Bio-Rad, France). Each of the SARS-CoV-2
432 Spike proteins expressed with different mutations were coupled with different colored MagPlex
433 beads so that tests could be performed with a single protein bead per well or in a multiplexed
434 Luminex binding assay. Binding curves for antibody affinity measurements and the Spike-

435 ACE2 interaction assay were performed as previously described (16, 37) using anti-human IgG-
436 PE secondary antibody (OneLambda ThermoFisher; Cat # H10104; 1:100 dilution) for antibody
437 detection in Spike Luminex binding assay and anti-mouse IgG-PE secondary antibody
438 (OneLambda ThermoFisher; Cat# P-21129; 1:100 dilution) in the Spike-ACE2 surrogate
439 neutralization assay. Competitive binding studies were performed by pre-incubating 25 µg/ml
440 of the indicated competitor antibody with the original 2019-nCoV Spike trimer protein coupled
441 Luminex beads for 30 minutes. Biotinylated P4J15, P2G3, AZD8895, AZD1061,
442 bebtelovimab, ADG-2 or sotrovimab antibodies (prepared as described above) were added to
443 each well at 1 µg/ml followed by a further 20-minute incubation. Biotinylated antibody bound
444 to RBD in the presence of competitor was stained with Streptavidin-PE at a 1:1000 dilution
445 (BD Biosciences) and analysed on a 200 Bioplex instruments. COVID-19 serum samples from
446 20 donors were monitored for levels of IgG antibody binding to the SARS-CoV-2 Spike trimer
447 proteins from 2019-nCoV, D614G, Alpha, Beta, Delta, Omicron BA.1 and BA.4 in the
448 Luminex bead-based assay.

449 **Anti-Spike B cell sorting, immortalization and cloning**

450 The bloods from ImmunoVax study donors were collected in EDTA tubes and the isolation of
451 blood mononuclear cells was performed using Leucosep centrifuge tubes (Greiner Bio-one)
452 prefilled with density gradient medium (Ficoll-Paque™ PLUS, GE Healthcare) according to
453 the manufacturer's instructions. Freshly isolated cells were stained with the cocktail of
454 fluorescent conjugated antibodies containing mouse anti-human CD19 APC-Cy7 (BD
455 Biosciences; Cat#557791; Clone SJ25C1; 5 µl titration in 100 µl), mouse anti-human CD3-
456 BV510 (BD Biosciences; Cat#563109; Clone UCHT1; 1 µl titration), mouse anti-human IgM-
457 FITC (Biolegend; Cat#314506; clone MHM-88; 2 µl titration), mouse anti-human IgD PE-
458 CF594 (BD Biosciences; Cat#562540; Clone IA6-2; 3 µl titration), mouse anti-human CD27-
459 APC (BD Biosciences; Cat#558664; Clone: M-T271; 5 µl titration), mouse anti-human CD38-
460 V450 (BD Biosciences; Cat#646851; Clone HB7; 5 µl titration) mAbs were used for antigen
461 specific B cell sorting along with the pre-complexed Omicron BA.1 variant Spike tetramer (2
462 µg in 100µl) coupled to PE-streptavidin (BD Biosciences; Cat#SA10044; 4:1 molar ratio). All
463 other aspects with cell sorting, immortalization protocol using EBV positive supernatants from
464 B95-8 cells and cloning were as described in Fenwick et al (21). Sequences for mAbs P4J15
465 are provided in PDB submissions PDB-8PQ2 and EMD-17819.

466 **SARS-CoV-2 live virus stocks**

467 All biosafety level 3 procedures were approved by the Swiss Federal Office of Public Health.
468 The SARS-CoV-2 BA.2.75.2 (EPI_ISL_14795784) and BQ.1 (EPI_ISL_15369810) isolates
469 were a kind gift from I. Eckerle, Geneva University Hospitals. Viral stocks were prepared in
470 EpiSerf (ThermoFisher Scientific, USA) with a single passage on VeroE6 cells, aliquoted,
471 frozen, titrated on VeroE6 cells by conventional plaque forming units and sequence verified.
472 BA.2.75.2 isolate differed from our cloned BA.2.75.2 ORF by 1 supplemental mutation
473 (G181V) already found in the original virus isolated from the patient.

474 **Selection of resistant virus in presence of mAbs**

475 The day before infection, HEK293T ACE2/TMPRSS2 cells previously described (22) were
476 seeded in 6-well plates coated with poly-L-lysine at a density of 1×10^6 cells per well. To
477 generate a viral population under mAb pressure, early passage virus was diluted in 1.5 ml
478 EpiSerf 2% FCS and incubated with 0.5 ng/ml mAb for 1 hr at 37°C in duplicates. Each mixture
479 was added to the cells and P1 (passage 1) supernatants were harvested 3 days later, clarified on
480 0.45 μ m SPIN-X centrifuge tube filters at 4000 \times g for 4 minutes. Aliquots of cleared P1
481 supernatants were diluted 1:40 in DMEM 2%, incubated with mAbs as described above and
482 used to infect fresh cells for 4 days. P2 supernatants were treated as P1 and P3 supernatants
483 were collected for RNA extraction and subsequent selection step. To select for mAb resistant
484 viruses, 200 μ l of the cleared undiluted P3 heterogeneous viral population was incubated with
485 200 μ l mAbs at 2.5 or 10 μ g/ml final concentration for 1 hr at 37°C. Mixture was then applied
486 on cells in 800 μ l DMEM 2% (1:2 volume) for 3 to 4 days. Viruses were selected one more
487 time and aliquots of passage 5 were used for RNA extraction and sequencing. Virus produced
488 in absence of mAb was collected and treated the same way in parallel to control for appearance
489 of mutations due to cell culture adaptation.

490 **Spike-pseudotyped vectors production and neutralization assays**

491 HDM-IDT Spike-fixK plasmid (BEI catalogue number NR-52514, obtained from J.D. Bloom,
492 Fred Hutchinson Cancer Research Centre) was used as backbone for all the cloning. The
493 cloning of D614G, Alpha, Beta and Delta clones have previously been described (22).
494 Pseudoviruses were alternatively produced with the original 2019-nCoV (Cat #100976), Alpha
495 / B.1.1.7 (Cat #101023) and Beta/B.1.351 (Cat #101024) pCAGGS-SARS2-Spike vectors
496 obtained from NIBSC. Omicron ORFs have been cloned with 1kb gBlocks assembly (IDT
497 DNA) followed by In-Fusion cloning in the same plasmid or were generated by gene synthesis
498 with a codon-optimized Spike ORF (Twist Biosciences). Escape mutations have been further

499 introduced by PCR-mediated mutagenesis. Pseudoviruses were produced by co-transfection
500 with pMDL p.RRE, pRSV.Rev and pUltra-Chili-Luc vectors (Addgene) into HEK 293T cells
501 as previously described (22).

502 SARS-CoV-2 pseudotyped VLPs have been produced by co-transfection of HDM-IDT Spike-
503 fixK, CoV-2 N, CoV-2-M-IRES-E and Luc-PS9 plasmids as described in Syed et al (38).
504 Briefly, for a 10-cm plate, plasmids CoV-2-N (0.67), CoV-2-M-IRES-E (0.33), HDM-
505 IDTSpike-fixK (0.03) and Luc-PS9 (1.0) at indicated mass ratios for a total of 20 µg of DNA
506 were diluted in 1 ml Opti-MEM (Gibco, ThermoFisher Scientific, USA). Then, 60 µg TransIT-
507 LT1 transfection reagent (Mirus Bio, USA) was added to plasmid dilution to complex the DNA,
508 according to the provider's instructions. Transfection mixture was incubated for 15 minutes at
509 room temperature and then added dropwise on HEK 293T cells in 10 ml of DMEM containing
510 10% foetal bovine serum. Media was changed after 18 hours of transfection. VLPs containing
511 media was collected 36 and 48 hours post transfection, pooled, centrifuged 5 minutes at 500 ×
512 g and the supernatants filtered using a 0.45 µm syringe filter. Samples were aliquoted and stored
513 at 4°C if used immediately or at -80°C for further analyses.

514 **RNA genome quantification**

515 Viral RNA was extracted from the supernatants with EZNA viral RNA extraction kit, DNase-
516 treated when particles were produced by transfection, reverse transcribed with Maxima H
517 Minus cDNA Synthesis Master Mix (ThermoFisher Scientific, USA) as recommended by the
518 manufacturer and the genome quantified by RT-qPCR performed in triplicates using the
519 following primers to detect either the Luciferase gene for VLPs or the RdP gene for viruses:
520 Luc(s): 5- GTG GTG TGC AGC GAG AAT AG -3' ; Luc(as): 5- CTG TTC AGC AGC TCG CGC
521 TC -3'; RdP(s): 5-AGC TTG TCA CAC CGT TTC-3', RdP(as): 5'-AAG CAG TTG TGG CAT
522 CTC-3' .

523 Absence of DNA contamination was always verified with a control amplification performed in
524 parallel in absence of reverse transcription step.

525 **Viral escapees sequencing and mapping**

526 Viral RNA was extracted from passage 5 supernatants and deep-sequenced. Sequencing reads
527 were mapped to the SARS-CoV-2 WuhCor1 strain downloaded from the UCSC database, using
528 botwie2 in sensitive mode with read gap penalties 5,1.9. The perbase package

529 (<https://github.com/sstadick/perbase>) was then used to obtain the nucleotide depth for each base
530 in the genome. Only mutations found in more than 20% of the reads were taken into accounts.

531

532 **Infectivity and neutralization assays of pseudotyped particles**

533 In each well of a black 96-well previously coated with poly-L-lysine (0.01% w/v solution,
534 Sigma-Aldrich USA), 50 µl of VLP-containing supernatants were added to 50 µl of cell
535 suspension containing 100 000 receiver cells (HEK293T ACE2/TMPRSS2 cells), in n=8
536 replicates. 24 hours later, supernatant was removed, then 30 µl of DMEM medium was added
537 with 30 µl of reconstituted luciferase assay buffer (Bright-Glo luciferase assay, Promega, USA)
538 and mixed. Luminescence was measured 5 minutes after using a Hidex Sense microplate reader
539 (Hidex Oy, Finland).

540 For lentiviral containing supernatants, the protocol is identical except the incubation time is 72
541 hrs instead of 24 hrs with assays performed as previously described (21).

542

543 **NHP challenge model for SARS-COV-2 Omicron BA.1 infection**

544 Cynomolgus macaques (*Macaca fascicularis*) originating from Mauritian AAALAC certified
545 breeding centres were used in this study. All animals were housed within IDMIT animal
546 facilities at CEA, Fontenay-aux-Roses under BSL-3 containment when necessary (Animal
547 facility authorization #D92-032-02, Préfecture des Hauts de Seine, France) and in compliance
548 with European Directive 2010/63/EU, the French regulations and the Standards for Human Care
549 and Use of Laboratory Animals, of the Office for Laboratory Animal Welfare (OLAW,
550 assurance number #A5826-01, US). Animals tested negative for *Campylobacter*, *Yersinia*,
551 *Shigella* and *Salmonella* before being use in the study.

552 The protocols were approved by the institutional ethical committee “Comité d’Ethique en
553 Expérimentation Animale du Commissariat à l’Energie Atomique et aux Energies Alternatives”
554 (CEtEA #44) under statement number A20-011. The study was authorized by the “Research,
555 Innovation and Education Ministry” under registration number APAFIS#29191-
556 2021011811505374 v1. All information on the ethics committee is available at
557 [https://cache.media.enseignementsup-recherche.gouv.fr/file/utilisation_des_animaux_fins_](https://cache.media.enseignementsup-recherche.gouv.fr/file/utilisation_des_animaux_fins_scientifiques/22/1/comiteethiqueea17_juin2013_257221.pdf)
558 [scientific/22/1/comiteethiqueea17_juin2013_257221.pdf](https://cache.media.enseignementsup-recherche.gouv.fr/file/utilisation_des_animaux_fins_scientifiques/22/1/comiteethiqueea17_juin2013_257221.pdf).

559 In the prophylactic protection study, ten female cynomolgus macaques aged 26-27 months at
560 the beginning of the study were randomly assigned between the control and treated groups to
561 evaluate the efficacy of P4J15 LS in protecting from challenge with the SARS-CoV-2 XBB.1.5
562 virus (NIH/BEI reference: NR-59105; hCoV-19/USA/MD-HP40900/2022). The treated group
563 (n = 6) received one dose at 5 mg/kg of P4J15 LS human IgG1 monoclonal antibody delivered
564 by intravenous slow bolus injection over 3-8 minutes three day prior to challenge, while control
565 animals (n = 4 in parallel and n=2 historical) received no treatment. The two historical control
566 animals were male and infected three weeks before the study with P4J15 LS. All animals were
567 then exposed to a total dose of 10^5 TCID₅₀ of Omicron XBB.1.5 SARS-CoV-2 virus produced
568 in Vero-ACE2-TMPRSS2 (NIH/BEI reference: NR-59105) via the combination of intranasal
569 and intratracheal routes with sample collection and testing performed as previously described
570 (39). Tracheal swabs, nasopharyngeal swabs and bronchoalveolar lavages were performed on
571 all NHPs collected throughout the study to monitor levels of both genomic and subgenomic
572 RNA for the SARS-COV-2 virus as previously described (40). All animals and data points were
573 included in the analysis. The NHP sample size was selected based on the large, 1- to 2-log
574 reduction in viral RNA anticipated in the trachea, nasopharyngeal and/or BAL with an effective
575 therapy that can provide statistically significant differences between treated and untreated
576 NHPs. These sample size assumptions were confirmed with the statistical differences observed
577 in viral RNA in viral RNA levels was evaluated using the Mann-Whitney two-sided tests to
578 compare control and treatment groups.

579 **Hamster challenge model SARS-CoV-2 infection**

580 KU LEUVEN R&D has developed and validated a SARS-CoV-2 Syrian Golden hamster
581 infection model that is suitable for the evaluation of potential antiviral activity of novel
582 antibodies (41-43). The SARS-CoV-2 strain used in this study was the Omicron BA.5 variant
583 (BA.5.2.1) [EPI_ISL_14782497] was isolated from nasopharyngeal swabs taken from patient
584 in Belgium. The variant was isolated in Vero E6 then passage 2 virus on Calu-3 cells was used
585 for the study described here and the genetic sequence of the stock was confirmed by deep
586 sequencing analysis. The titer of the virus stock was determined by end-point dilution on Vero
587 E6 cells by the Reed and Muench method. Live virus-related work was conducted in the high-
588 containment A3 and BSL3+ facilities of the KU Leuven Rega Institute (3CAPS) under licenses
589 AMV 30112018 SBB 219 2018 0892 and AMV 23102017 SBB 219 20170589 according to
590 institutional guidelines. Vero E6 cells (African green monkey kidney, ATCC CRL-1586) were
591 cultured in minimal essential medium (Gibco) supplemented with 10% fetal bovine serum

592 (Integro), 1% L- glutamine (Gibco) and 1% bicarbonate (Gibco). End-point titrations were
593 performed with medium containing 2% fetal bovine serum instead of 10%.

594 The hamster infection model of SARS-CoV-2 has been described before (41, 43). In brief,
595 wild-type Syrian Golden hamsters (*Mesocricetus auratus*) were purchased from Janvier
596 Laboratories and were housed per two in ventilated isolator cages (IsoCage N
597 Biocontainment System, Tecniplast) with ad libitum access to food and water and cage
598 enrichment (wood block). The animals were acclimated for 4 days prior to study start.
599 Housing conditions and experimental procedures were approved by the ethics committee
600 of animal experimentation of KU Leuven (license P065-2020). Female hamsters of 6-8 weeks
601 old were administered IgG1 isotype control (5 mg/kg), P4J15 LS (5 mg/kg, 1 mg/kg or 0.5
602 mg/kg) or bebtelovimab (5 mg/kg) by intraperitoneal injection. Two days later, hamsters were
603 anesthetized with ketamine/xylazine/atropine, blood samples were collected, and animals were
604 inoculated intranasally with 100 μ L containing 1×10^4 n tissue culture infectious dose (TCID₅₀)
605 of SARS-CoV-2 Omicron BA.5 (day 0). Hamsters were monitored for appearance, behaviour
606 and weight. Antibody concentrations present in the hamster plasma on day 0 of the study were
607 performed using the Luminex assay described above with Spike trimer coupled beads and using
608 purified P4J15 LS antibody to generate a standard curve. In these studies, no control animals
609 were excluded. In treated groups, animals with undetectable levels of serum antibodies (one
610 hamsters in the 5 mg/kg P4J15 LS group and 2 hamsters in the 1 mg/kg P4J15 LS group) were
611 excluded from the analysis as this indicated a technical failure in the drug administration. At
612 day 4 post infection, hamsters were sacrificed, and lung tissues were homogenized using bead
613 disruption (Precellys) in 350 μ l TRK lysis buffer (E.Z.N.A. Total RNA Kit, Omega Bio-tek)
614 and centrifuged (10,000 rpm, 5 min) to pellet the cell debris. RNA was extracted according to
615 the manufacturer's instructions. Of 50 μ l eluate, 4 μ l was used as a template in RT-qPCR
616 reactions. RT-qPCR was performed on a LightCycler96 platform (Roche) using the iTaq
617 Universal Probes One-Step RT-qPCR kit (BioRad) with N2 primers and probes targeting the
618 nucleocapsid (41). Standards of SARS-CoV-2 cDNA (IDT) were used to express viral genome
619 copies per mg tissue. For end-point virus titrations, lung tissues were homogenized using bead
620 disruption (Precellys) in 350 μ l minimal essential medium and centrifuged (10,000 rpm, 5min,
621 4°C) to pellet the cell debris. To quantify infectious SARS- CoV-2 particles, endpoint titrations
622 were performed on confluent Vero E6 cells in 96- well plates. Viral titers were calculated by
623 the Reed and Muench method using the Lindenbach calculator and were expressed as 50%
624 tissue culture infectious dose (TCID₅₀) per mg tissue. The hamster sample size was selected

625 based on the large, >1-log reduction in viral RNA and infectious virus anticipated in the lung
626 tissue with an effective therapy that can provide statistically significant differences between
627 treated and untreated animals. These sample size assumptions were confirmed in our statistical
628 analysis. Statistical differences in viral RNA levels and infectivity were evaluated using the
629 Mann-Whitney two-sided tests to compare control and treatment groups.

630 **Cryo-electron microscopy**

631 Cryo-EM grids were prepared with a Vitrobot Mark IV (ThermoFisher Scientific). Quantifoil
632 R1.2/1.3 Au 400 holey carbon grids were glow-discharged for 90s at 15mA using a GloQube
633 Plus Glow-Discharge System (Quorum, Inc.). 2.0 μ l of a 2.1 mg/ml XBB.1 Spike was mixed
634 with 2.0 μ l of a 0.28 mg/ml P4J15 Fab fragments (Final 11.1 μ M XBB.1 Spike:5.6 μ M P4J15
635 Fab) and 3.0 μ l of the fresh complex was applied to the glow-discharged grids, blotted for 4s
636 under blot force 10 at 95% humidity, wait time 10s and 10 °C in the sample chamber, and then
637 the blotted grid was plunge-frozen in liquid nitrogen-cooled liquid ethane.

638 Grids were transferred in a ThermoFisher Scientific Titan Krios G4 transmission electron
639 microscope, equipped with a Cold-FEG on a Falcon IV detector (Dubochet Center for Imaging,
640 Lausanne) in electron counting mode. Falcon IV gain references were collected just before data
641 collection. Data was collected using TFS EPU v2.12.1 using aberration-free image shift
642 protocol (AFIS), recording 4 micrographs per ice hole. A total of 24 814 micrographs in EER
643 format were recorded at magnification of 165kx, corresponding to the 0.83Å pixel size at the
644 specimen level, with defocus values ranging from -0.6 to -2.0 μ m. Exposures were adjusted
645 automatically to 50 $e^-/\text{Å}^2$ total dose.

646

647 **Cryo-EM image processing**

648 During the data acquisition phase, on-the-fly processing was employed to assess the data quality
649 for screening purposes, utilizing cryoSPARC live v3.3.1 (44). Raw stacks were subjected to
650 motion correction without binning, utilizing cryoSPARC's implementation of motion correction
651 and contrast transfer function estimation (45). A total of 6,769,807 particles were automatically
652 template-picked. Following several rounds of 2D classification, 362,329 particles were selected
653 and utilized for ab-initio reconstruction and 3D classifications. Within this dataset, multiple
654 conformers were identified; however, after thorough validation, a subset of 95,910 particles
655 corresponding to a P4J15 fragment bound to an XBB1 trimer was deemed reliable.

656 Homogeneous refinement using the selected particles resulted in a 3D reconstruction at a
657 resolution of 3.01 Å (FSC 0.143) with C1 symmetry. To further enhance the map quality,
658 focused refinement was performed using a soft mask volume encompassing an RBD-up region
659 and its bound Fab. This refinement process yielded a final Coulomb map at 3.85 Å resolution
660 (FSC 0.143) with C1 symmetry (**Supplementary Fig. 4**). The soft mask volumes were
661 manually generated in UCSF ChimeraX (46) and the Cryosparc Volume tool. Post-processing
662 polishing was conducted with EMReady (23) to improve the map quality and aid in resolving
663 any atom position ambiguities. Finally, the building and refinement steps were exclusively
664 carried out using CryoSPARC maps.

665 **Cryo-electron microscopy model building**

666 To generate initial models of the P4J15 Fab and XBB1 spike, various approaches were
667 employed. These included utilizing models from the Spike trimer (PDB ID 7QO7), AlphaFold2
668 (implemented through ColabFold), and ModelAngelo 0.3 (47) for sequence-based generation.
669 The cryo-EM maps were fitted with the Spike trimer using UCSF ChimeraX, serving as the
670 starting point for further manual refinement. Manual extension and building of the docked
671 models were carried out using Coot 0.9.8 (48). To refine the models, Phenix 1.20 (49) was
672 employed. The generated figures depicting the models were prepared using UCSF ChimeraX.
673 The numbering scheme for the full-length Spike models within the global map is based on
674 Omicron numbering. For models containing only the RBD within the local maps, wild-type
675 numbering is utilized. In the case of the P4J15 Fab, the numbering of both the heavy and light
676 chains start from one, beginning with the CH1 and CL domains, respectively. For additional
677 analysis, buried surface area measurements were calculated using ChimeraX. Predictions
678 regarding hydrogen bonds and salt bridges were performed using PDBePISA.

679 **Statistical analysis**

680 Statistical parameters including the exact value of n, the definition of centre, dispersion, and
681 precision measures (Mean or Median \pm SEM) and statistical significance are reported in the
682 Figures and Figure Legends. Data were judged to be statistically significant when $p < 0.05$. In
683 Figures, asterisks denote statistical significance as calculated using the two-tailed non-
684 parametric Mann-Whitney U test for two groups' comparison or with Kruskal-Wallis tests with
685 Dunn's multiple-comparison correction. Analyses were performed in GraphPad Prism
686 (GraphPad Software, Inc.) and Microsoft Excel.

687

688 **Data availability**

689 All data supporting the findings of this study are available within the paper and in the Source
690 Data. The reconstructed maps of the global Omicron Spike with Fabs bound are available from
691 the EMDB database, C1 symmetry, EMD-17819. The atomic model for the RBD-up with one
692 Fabs bound in the locally refined map is available from the PDB database, PDB-8PQ2. All
693 plasmids made in this study are available upon request to the corresponding authors.

694

695 **Declaration of Competing Interest**

696 C.F., G.P., P.T. and D.T. are co-inventors on a patent application that encompasses the
697 antibodies and data described in this manuscript (EP 22199188.8). DT and GP are amongst the
698 founders of and own equity in Aerium Therapeutics, which has rights to and is pursuing the
699 development of the antibodies described in the publication and has a Sponsored Research
700 Agreements with the Lausanne University Hospital (CHUV) and the Ecole Polytechnique
701 Fédérale de Lausanne (EPFL). The remaining authors declare no competing interests.

702

703 **Acknowledgements**

704 We thank the Vaccinology and Immunotherapy Centre (VIC) at the Service of Immunology
705 and Allergy of the Lausanne University Hospital for assistance with cell sorting; Laura Junges
706 and Laetitia Bossevot from IDMIT/CEA for qPCR in NHP samples. We thank Isabella Eckerle,
707 Meriem Bekliz and the Virology laboratory of Geneva University Hospital for the Omicron
708 RNA sample and variant isolates collection, the Geneva Genome Center for sequencing and
709 Evarist Planet for the viral sequences mapping. We thank Laurence Durrer, Rosa Schier,
710 Michaël François and Soraya Quinche from the EPFL Protein Production and Structure Core
711 Facility for mammalian cell production and purification of proteins, Alexander Myasnikov,
712 Bertrand Beckert and Sergey Nazarov from the Dubochet Center for Imaging (an EPFL,
713 UNIGE, UNIL initiative) for cryoEM grids preparation and data collection. We thank Julien
714 Lemaitre, Quentin Sconosciuti, Sébastien Langlois, Victor Magneron, Maxime Potier, Jean-
715 Marie Robert, Emma Burban, Eleana Navarre, Flavie Mispion and Tiphaine Bourgès for the
716 NHP experiments; Laura Junges and Kyllian Lheureux for the RT-qPCR. Elodie Guyon, Julien
717 Dinh and Eloise Joffroy for the NHP sample processing; Sylvie Legendre for the transport
718 organization; Frédéric Ducancel, Alicia Pouget and Yann Gorin for the logistics and safety
719 management; Isabelle Mangeot and Salome Piault for help with resources management and
720 Brice Targat and Karl-Stefan Baczowski who contributed to data management. The virus stock
721 used for the NHPs was obtained from the Biodefense, Research Resources, and Translational
722 Research branches of the NIH/NIAID/DMID/OBRRTR/RRS (Program Officer, Clint Florence,
723 Ph.D.). The Infectious Disease Models and Innovative Therapies research infrastructure
724 (IDMIT) is supported by the “Programme Investissements d’Avenir” (PIA), managed by the
725 ANR under references ANR-11-INBS-0008 and ANR-10-EQPX-02-01. We would also like
726 to thank Trudi Veldman and members of the CARE-IMI work package 4 team for helpful
727 discussions.

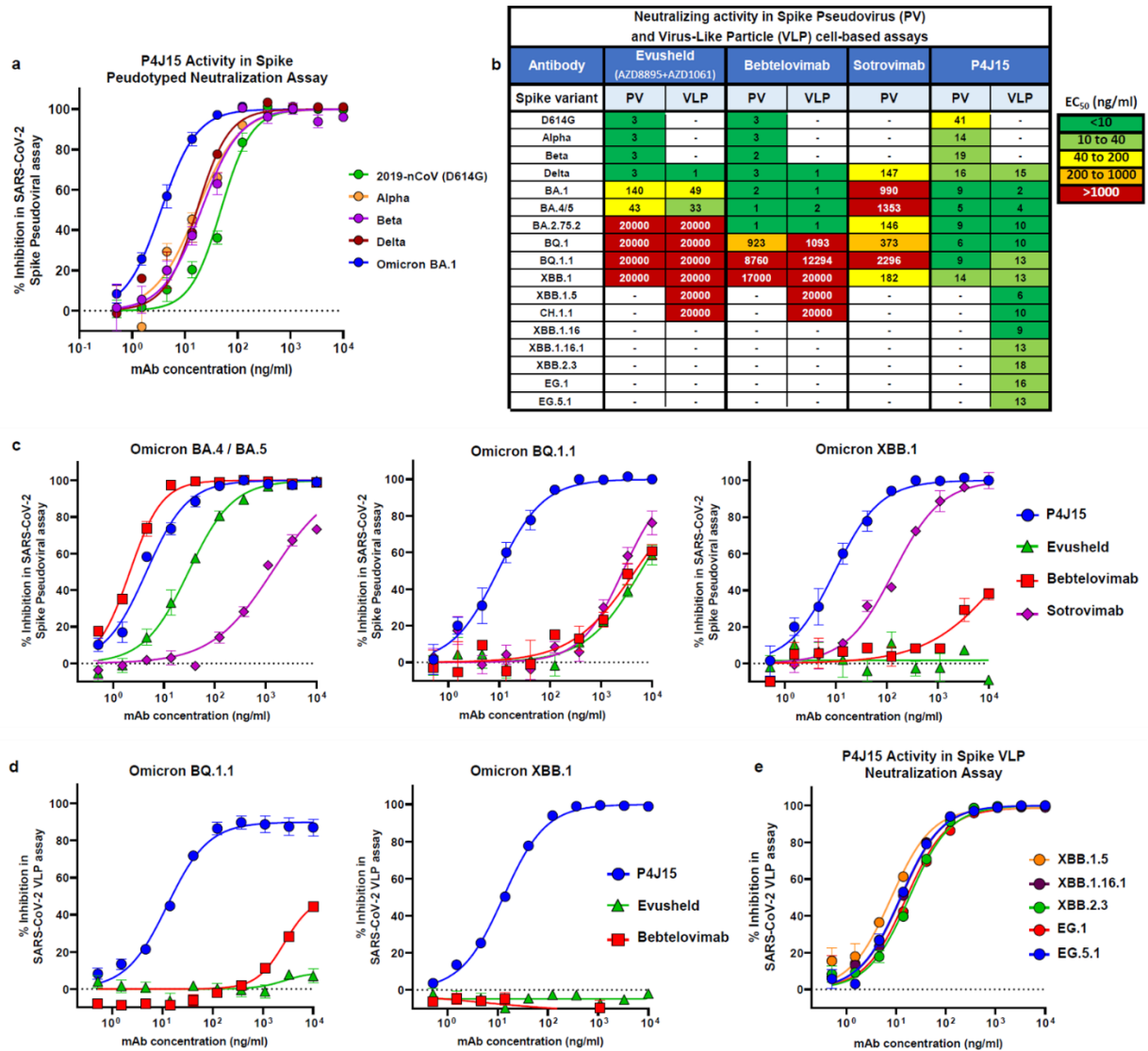
728 **Funding:** This work was supported by the Corona Accelerated R&D in Europe (CARE) project
729 funded by the Innovative Medicines Initiative 2 Joint Undertaking (JU) under grant agreement
730 No 101005077. The JU receives support from the European Union’s Horizon 2020 research
731 and innovation program, the European Federation of Pharmaceutical Industries Associations
732 (EFPIA), the Bill & Melinda Gates Foundation, Global Health Drug Discovery Institute and
733 the University of Dundee. The content of this publication only reflects the author’s view and
734 the JU is not responsible for any use that may be made of the information it contains (funding
735 to G.P. and R.L). G.P. and D.T. received support from the CoVICIS project (grant No.
736 10146041) funded by the European Union Horizon Europe Program. Additional funding was
737 provided through the Lausanne University Hospital (to G.P.), the Swiss Vaccine Research
738 Institute (to G.P. and NCCR TransCure to H.S.), Swiss National Science Foundation Grants (to
739 G.P.) and through the EPFL COVID fund (to D.T.) and a donation from a private foundation
740 advised by CARIGEST S.A. (to DT and GP).

741

742 **Author contributions**

743 C.F. designed the strategy for isolating and profiling anti-Spike antibodies, coordinated the
744 research activities, designed Spike variant constructs, analysed the data, wrote the initial draft
745 and contributed to the editing of the manuscript. P.T. established, performed the experiments
746 with live SARS-CoV-2 virus and designed the Spike protein mutations with the help of C.R.,
747 analysed the results and contributed to the editing of the manuscript. C.R. and V.G. performed
748 Spike cloning and VLP-based experiments. M.L. sets up the SARS-CoV-2 VLPs assay. Y.D.,
749 K.L., F.P., L.P., and H.S. coordinated the cryo-EM analysis, analysed the structural data and
750 contributed to the editing of the manuscript. Other contributed as follows: L.E.-L., performed
751 the B cells sorting, immortalization, binding studies and mAb functional assays; A.F. and J.Ce.,
752 cloning of mAb VH and HL, and generation of Omicron BA.5 mutations by site directed
753 mutagenesis; J.Ca., binding studies, production of lentiviruses and pseudoviral assays; F.F.
754 mAb purification, mAb characterization and molecular biology; F.P. coordinated production of
755 recombinant Spike protein and mAb. P.L., Y.L. and R.L. designed the *in vivo* studies, which
756 were executed by C.H, R.M., N. D.-B., F.R., R.A., C.S.F., G.V. and J.N. G.P. and D.T.
757 conceived the study design, analysed the results and wrote the manuscript.

758 **Figures**



759

760 **Figure 1: P4J15 exhibits potent and broad neutralizing activity against spike-coated**
 761 **pseudoviruses**

762 **a)** Neutralization of lentiviral particles pseudotyped with SARS-CoV-2 Spike expressing the
 763 ancestral 2019-nCoV (D614G), Alpha, Beta, Delta or Omicron BA.1 variants of concern in
 764 HEK293T ACE2/TMPRSS2 cell infection assays. Replicates in concentration response curves
 765 were n=6 for all Spike pseudoviruses. **b)** Heatmap table showing EC₅₀ neutralization potencies
 766 for P4J15 and reference antibodies Evusheld (combination of AZD8895 and AZD1061),
 767 bebtelovimab and sotrovimab evaluated in spike-coated pseudovirus and SARS-CoV-2 virus-
 768 like particle cell-based assays. **c)** Concentration response inhibition curves for Omicron BA.4/
 769 BA.5, BQ.1.1 and XBB.1 Spike pseudotyped lentivirus cell-based neutralization assays (n=6).
 770 **d)** Concentration response inhibition curves for Omicron BQ.1.1 and XBB.1 Spike
 771 pseudotyped SARS-CoV-2 VLP cell-based neutralization assays (n=8 for Evusheld and n=12

772 for remaining mAbs). e) Concentration response inhibition curves for P4J15 in XBB.1.5,
773 XBB.1.16, XBB.1.16.1, XBB.2.3 and EG.1 Spike pseudotyped VLP cell-based neutralization
774 assays (n=4). Mean values \pm SEM are shown.

775

776

777

778

779

780

781

782

783

784

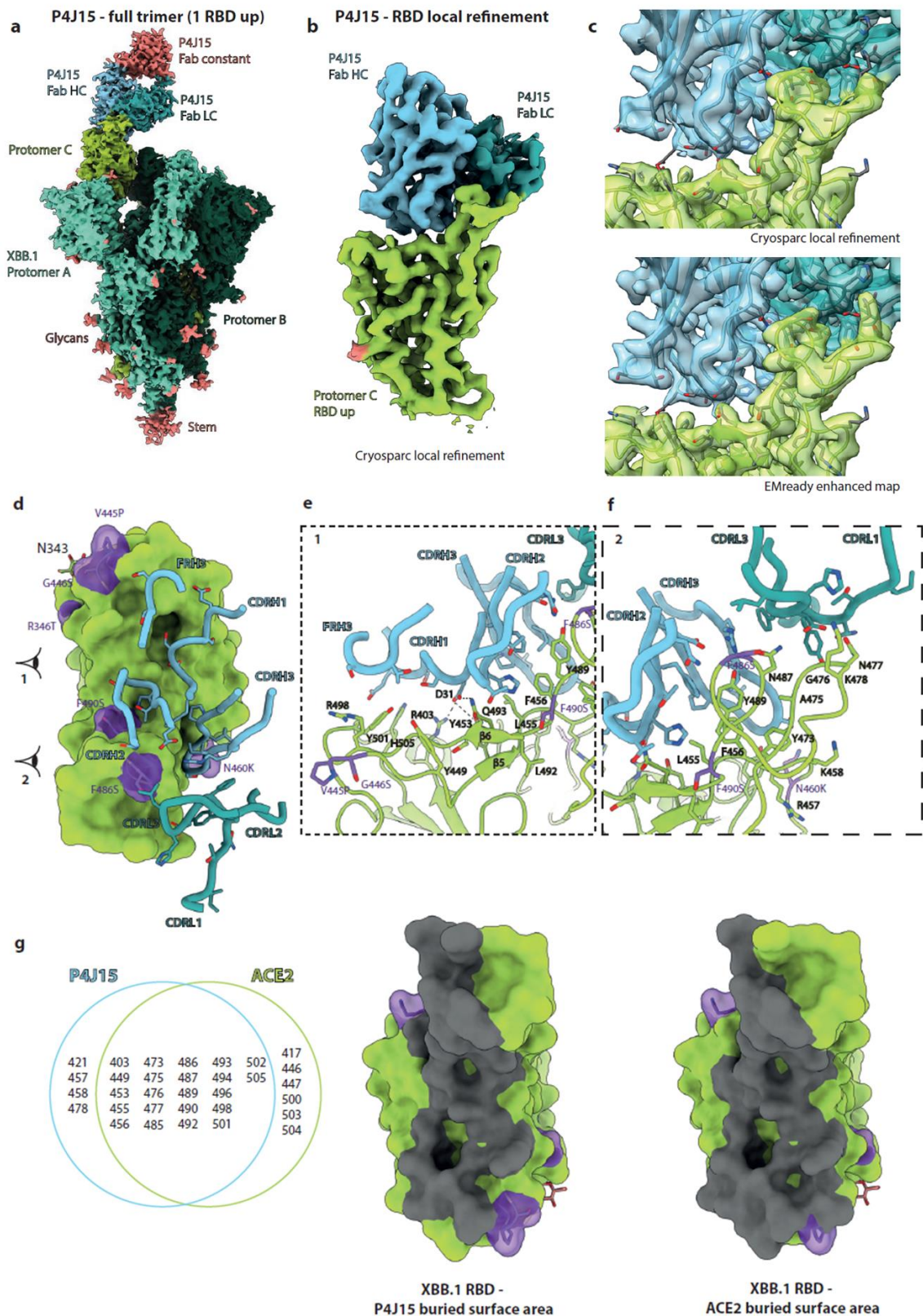
785

786

787

788

789



790

791 **Figure 2. P4J15 binds the full-length Omicron Spike**

792 a) Cryo-EM composite density map of the full-length Omicron XBB.1 Spike bound to one
 793 P4J15 Fab fragment. Spike protomers are colored in light green, green and dark green, while

794 P4J15 heavy chain variable region is cyan, the light chain variable region turquoise and Fab
795 constant regions pink. **b)** Cryosparc local refinement map of RBD in the up configuration (light
796 green) bound by P4J15 heavy and light chains. **c)** Zoomed-in view of RBD – P4J15 interaction
797 with ribbon structure representation of both and semi-transparent surface representations of
798 cryosparc local refinement and EMReady enhanced maps, shown in top and bottom panels,
799 respectively. **d)** Top view representation of the RBD in green and P4J15 heavy and light chain
800 contact loops shown in cyan and turquoise, respectively. **e)-f)** Front view of the RBD
801 interaction region with P4J15 as indicated by the eye 1 and eye 2 as shown in panel d) for e)
802 and f), respectively. RBD is represented as a ribbon structure in green, while P4J15 heavy chain
803 CDRs and frame region 3 (FRH3) are shaded cyan and light chain CDRs are shaded turquoise.
804 Key RBD and P4J15 contact residues are labelled and represented in stick format. **g)** Venn
805 diagram showing common contact residues on RBD shared between P4J15 and ACE2. Buried
806 surface area for P4J15 and ACE2 are shaded dark grey on the green space filled representation
807 of the RBD. In panels d) and g), the XBB.1 mutations relative to Omicron BA.4 are shaded
808 purple.

809

810

811

812

813

814

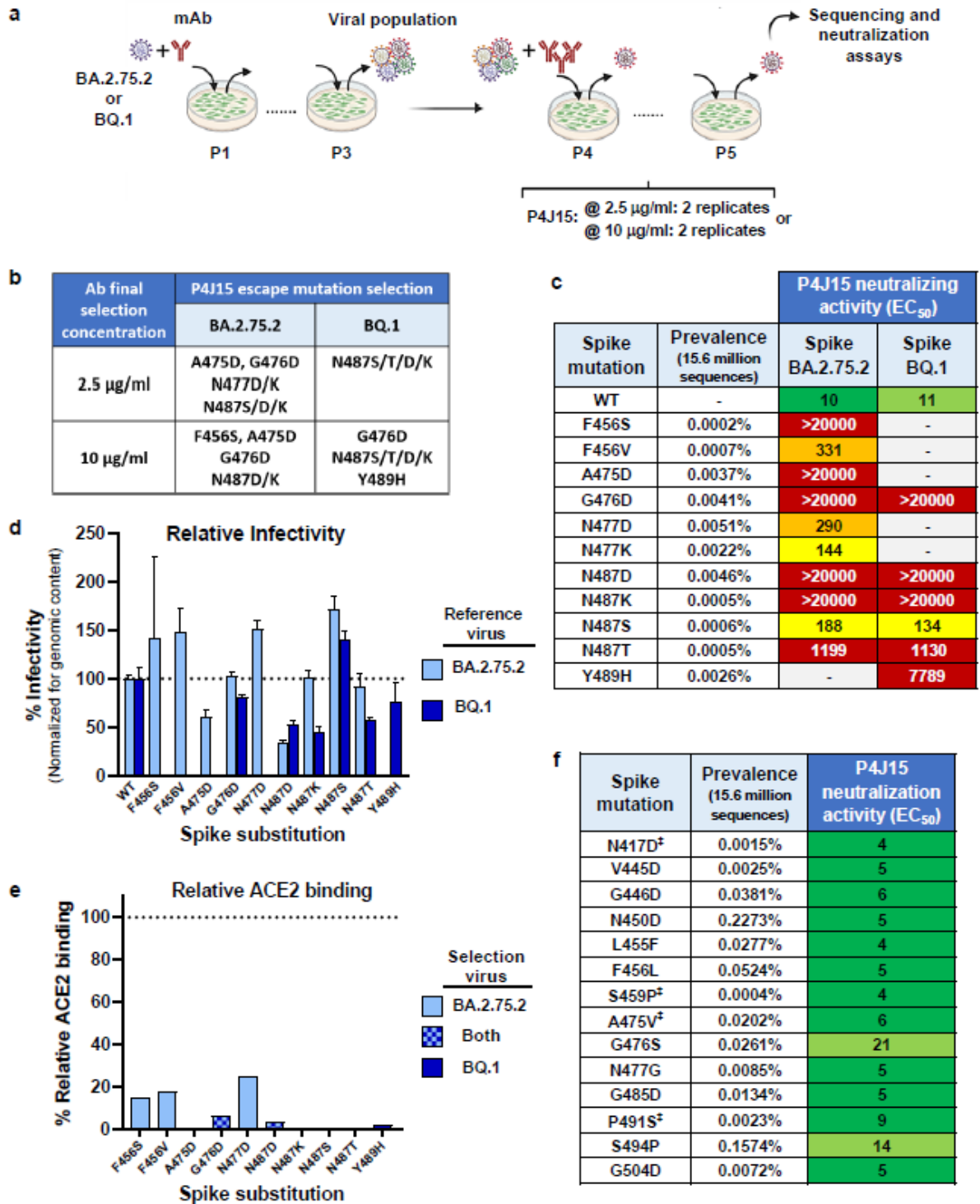
815

816

817

818

819

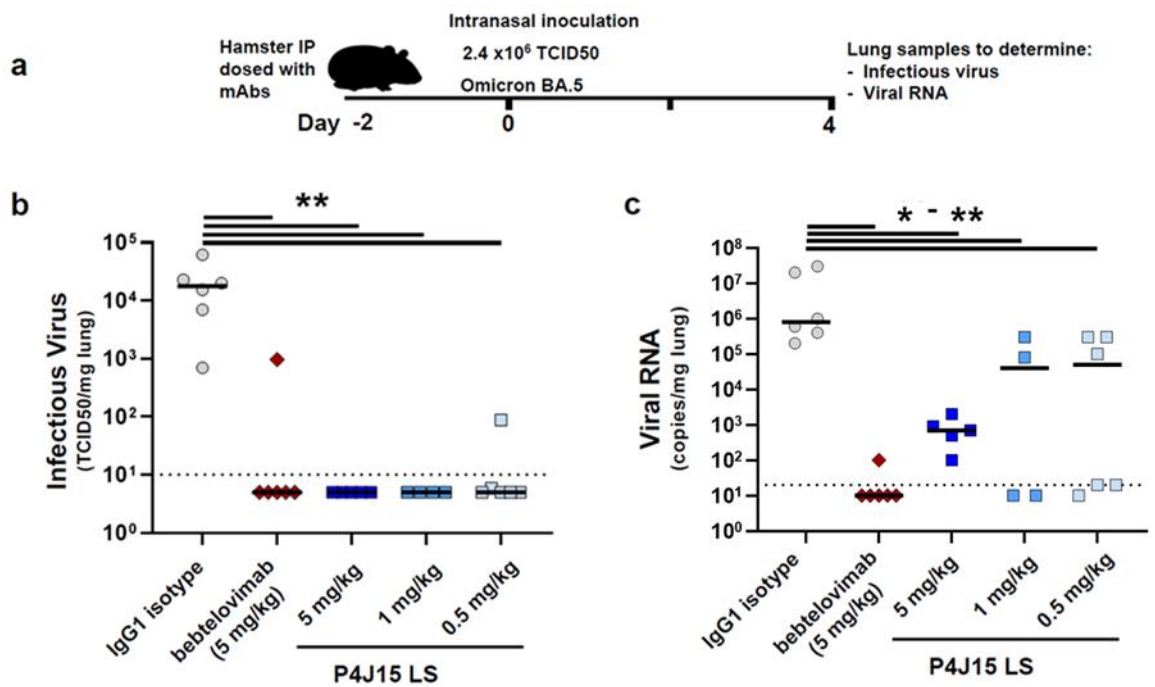


820

821 **Figure 3: Identification and characterization of escape mutations to P4J15**

822 **a)** Schematic representation of escapees selection. Omicron BA.2.75.2 and BQ.1 replicative
 823 isolates were used to infect VeroE6 cells (MOI of 0.2) each in duplicates in presence of
 824 suboptimal concentrations of antibodies. Supernatants were collected, diluted 40-fold and used
 825 to infect cells for two more passages in the same conditions (P1 to P3). Putative viral escapees
 826 were further selected by serial passages of 2-fold diluted supernatants pre-incubated with high

827 concentrations of antibodies (two concentrations, each tested in duplicates). Viral RNA
828 extracted from supernatants collected at passage 5 was deep-sequenced. **b)** Mutations identified
829 across escape selection experiments are indicated in the table. **c)** Prevalence in GISAID
830 sequence database is indicated for each identified mutation. BA.2.75.2 or BQ.1 Spikes were
831 mutated accordingly with the identified residues and pseudotyped VLPs produced and tested in
832 conventional neutralization assays. Heatmap table overviews the EC₅₀ value neutralizing
833 potency of P4J15 against the different VLPs. **d)** Infectivity of the VLPs pseudotyped with the
834 different Spike mutations is shown relative to the parent VLP produced with either BA.2.75.2
835 or BA.1 Spike. Transduction efficiency was monitored by Luciferase activity in the VLPs
836 transduced HEK293T ACE2/TMPRSS2 cells (n= 16 for all except for G476D and N487
837 mutations where each have been tested in n=8 replicates). Infectivity is given for the same
838 amount of each infectious VLP as determined by genome content of the stocks. Mean values ±
839 SD are shown, and Kruskal-Wallis test shows significantly reduced infectivity of A475D,
840 N487D (p=0.0065 and p<0.0001, respectively) for BA.2.75.2 VLPs and N487D, N487K,
841 N487T (each p<0.0001) for BQ.1 VLPs. **e)** Relative binding of ACE2 to RBD with the indicated
842 amino acid substitutions as determined using the ACE2-RBD interactive tool developed by
843 Jesse Bloom's laboratory with Omicron BA.2 used as the reference variant. **f)** Pseudotyped
844 lentiviruses or VLPs produced with rare but most common amino acid substitutions at positions
845 identified at or near the P4J15-RBD contact site and in our resistance studies. Mutations were
846 incorporated in the Omicron BA.4 /BA.5 Spike for lentiviruses and BQ.1 Spike for VLPs
847 (indicated by ‡) with the prevalence in the GISAID sequence database indicated of each variant
848 substitution. Heatmap tables (with same color ranges as in Figure 1b) overviews the neutralizing
849 potency of P4J15 against the different pseudotyped lentiviruses (n=6) and VLPs (n=4).



850

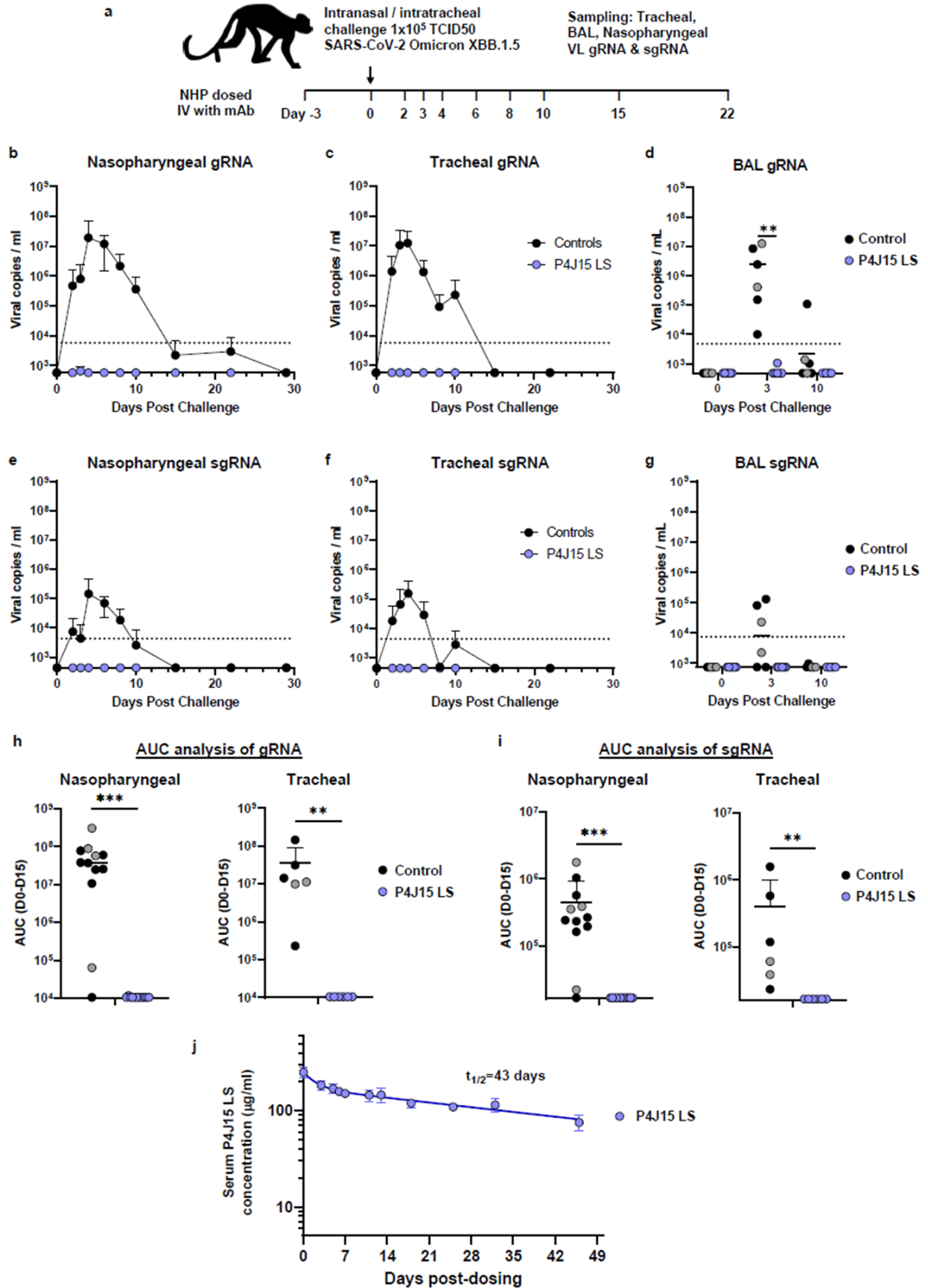
851

852 **Figure 4: *In vivo* efficacy in the SARS-CoV-2 Omicron BA.5 hamster challenge model**

853 **a)** Overview of study design for the SARS-CoV-2 hamster challenge model. Animals were
 854 administered intraperitoneally 5.0, 1.0 or 0.5 mg/kg of P4J15, 5 mg/kg of bebtelovimab positive
 855 control or 5 mg/kg of an IgG1 isotype control and challenged two days later (Day 0) with an
 856 intranasal inoculation of the Omicron BA.5 SARS-CoV-2 virus (2.4×10^6 TCID₅₀). **b)** Median
 857 levels of infectious virus and **c)** viral RNA copies/mg lung tissue in each of the study arms are
 858 shown for day 4 post-inoculation with SARS-CoV-2 virus. A total of 4-6 hamsters were used
 859 per P4J15 treatment arm. Non-parametric Mann-Whitney two-tailed tests were used to evaluate
 860 the statistical difference between the treatment conditions with $P= 0.0043, 0.0043, 0.0095$ and
 861 $0.0022 (**)$ in **b** (left to right) and $P=0.0022, 0.0043, 0.0190$ and $0.0087 (* \text{ to } **)$ in **c** (left to
 862 right).

863

864



865

866

867 **Figure 5: *in vivo* efficacy of P4J15 against the SARS-COV-2 XBB.1.5 virus infection in**
868 **the non-human primate (NHP) challenge model**

869 **a)** Overview of study design for the SARS-CoV-2 NHP challenge model. Six animals were
870 administered intravenous 5 mg/kg of P4J15 LS and challenged three days later (Day 0) along
871 with four control animals (in black) via intranasal and intratracheal inoculation of the Omicron
872 XBB.1.5 SARS-CoV-2 virus (1×10^5 TCID₅₀). Tracheal fluids, nasopharyngeal fluids and
873 bronchoalveolar lavages (BAL) collected during the course of the study were evaluated for viral
874 copies per ml of genomic (g)RNA **b)-d)** and subgenomic (sg)RNA **e)-g)** with data plotted to
875 include two historical control animals (grey circles) infected with the same inoculum and batch
876 of Omicron XBB.1.5 virus. **h)** Area under the curve (AUC) analysis of gRNA detected
877 between days 0 and 15 of the study. Individual data for nasopharyngeal fluids collected from
878 left and right nostril for each of the timepoints (n=12) and tracheal fluids (n=6) were plotted in
879 left and right panels, respectively. **i)** AUC analysis of sgRNA detected between days 0 and 15
880 of the study for samples as indicated in h. **j)** Pharmacokinetic evaluation of P4J15 LS serum
881 concentrations with the terminal phase half-life determined using a two-phase exponential
882 decay analysis. Mean values \pm SD are shown, and Mann-Whitney two-sided tests were
883 performed to compare study groups in panels d, h, i with P values of 0.0022 (**) for d; and
884 $p < 0.0001$ (****) and 0.0022 (**) of h and i. Lower limit of detection were 2.76- and 2.63-log
885 copies per ml for viral gRNA and sgRNA, respectively. Dotted line indicates lower limit of
886 quantitation at 3.76- and 3.63-log copies per ml for viral gRNA and sgRNA, respectively.

887

888

889

890

891

892

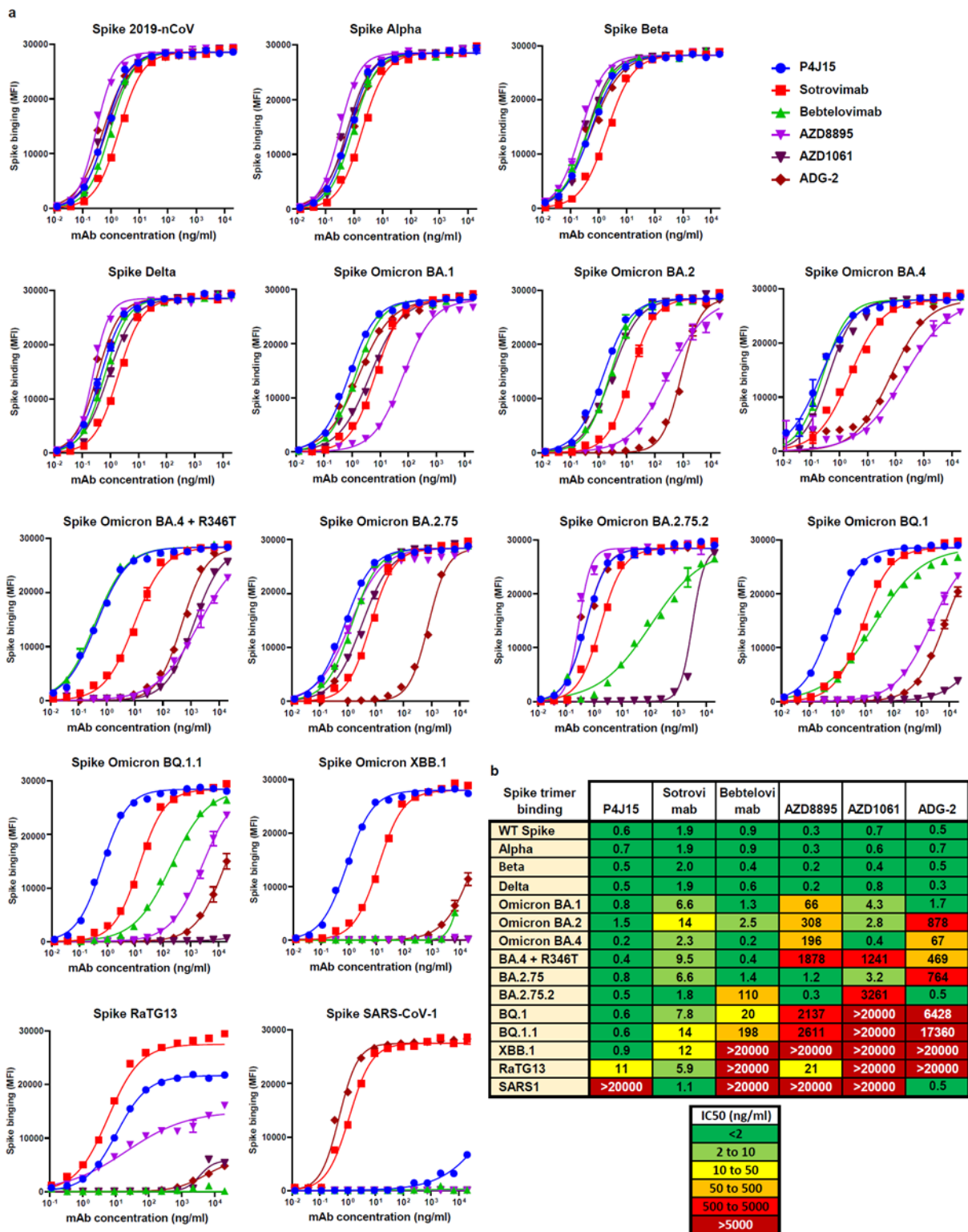
893

894

895

896

897 **Supplementary Figures:**



898

899 **Supplementary data Fig. 1 – Binding properties of P4J15 and other anti-SARS-CoV-2**
 900 **antibodies for recombinant Spike trimer proteins from SARS-CoV-2 2019-nCoV to**
 901 **Omicron XBB.1, and sarbecovirus RaTG13 and SARS-CoV-1 proteins.**

902 **a)** Spike binding curves performed in a Luminex bead-based assay. **b)** Heatmap table showing
903 binding affinity IC50 values for our panel of mAbs to the indicated Spike trimer proteins. Data
904 presented are representative of 2-4 independent experiments with each concentration response
905 tested in duplicate. Mean values \pm SEM are shown.

906

907

908

909

910

911

912

913

914

915

916

917

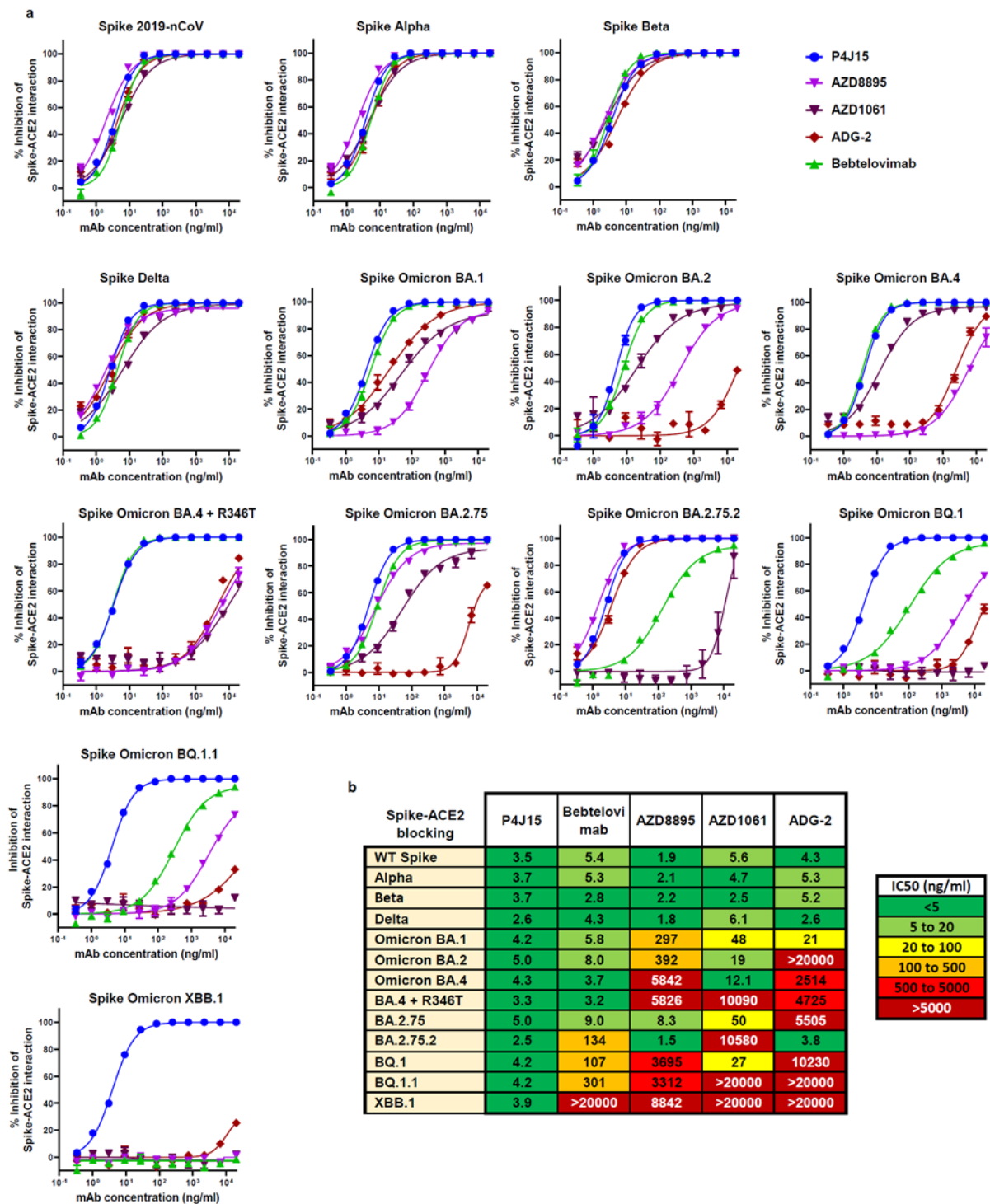
918

919

920

921

922



923

924 **Supplementary data Fig. 2 – P4J15 is the most potent and broadly active antibody in a**
 925 **Spike-ACE2 surrogate neutralization assay performed with trimeric Spike proteins from**
 926 **a panel of SARS-CoV-2 variants of concern.**

927 **a) Spike-ACE2 blocking activity of P4J15 compared to a panel of authorized and clinically**
 928 **advanced anti-Spike mAbs. b) Heatmap table showing IC₅₀ values for our panel of mAbs in the**
 929 **Spike-ACE2 assay. Luminex based assays were performed with beads coupled with Spike**

930 trimer proteins from the original 2019-nCoV SARS-CoV-2, Alpha, Beta, Gamma, and the
 931 different Omicron lineages listed. Sotrovimab was not included in this analysis as it binds the
 932 RBD without blocking the Spike-ACE2 interaction. Data presented is representative of 2-4
 933 independent experiments with each concentration response tested in duplicate. Mean values \pm
 934 SEM are shown.

935

936

937

938

Detection of biotinylated mAbs binding to the Spike trimer								
Competition mAb pre-bound to Spike trimer	P5C3 - Biotin	AZD 8895	P4J15 - Biotin	ADG-2 - Biotin	bebtelovimab - Biotin	AZD1061 - Biotin	P2G3 - Biotin	Sotrovimab - Biotin
P4J15	Red	Red	Red	Red	White	White	White	White
P5C3	Red	Red	Red	Orange	White	White	White	White
AZD8895	Red	Red	Red	White	White	White	White	White
ADG-2	Orange	White	White	Red	Red	Red	Red	Orange
Bebtelovimab	White	White	White	White	Red	Red	Red	Red
AZD1061	White	White	White	White	Red	Red	Red	Red
P2G3	White	White	White	White	Red	Red	Red	Red
Sotrovimab	White	White	White	White	Red	Red	Red	Red

Competitive <25% co-binding

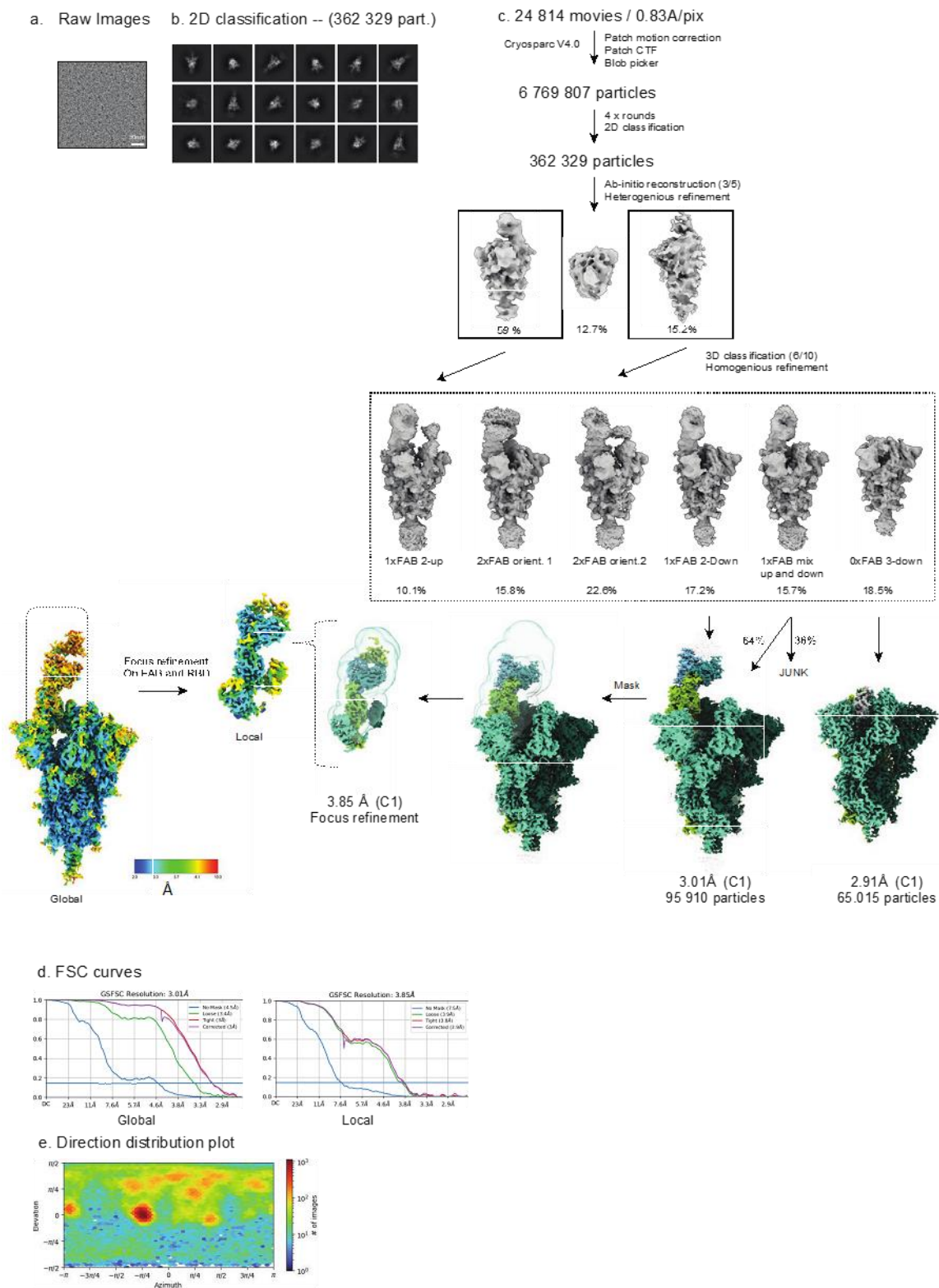
Partially competitive 25-70% co-binding

Non-competitive >70% co-binding

939

940 **Supplementary data Fig. 3 – P4J15 binds competitively to the Spike trimer with Class 1**
 941 **neutralizing antibodies**

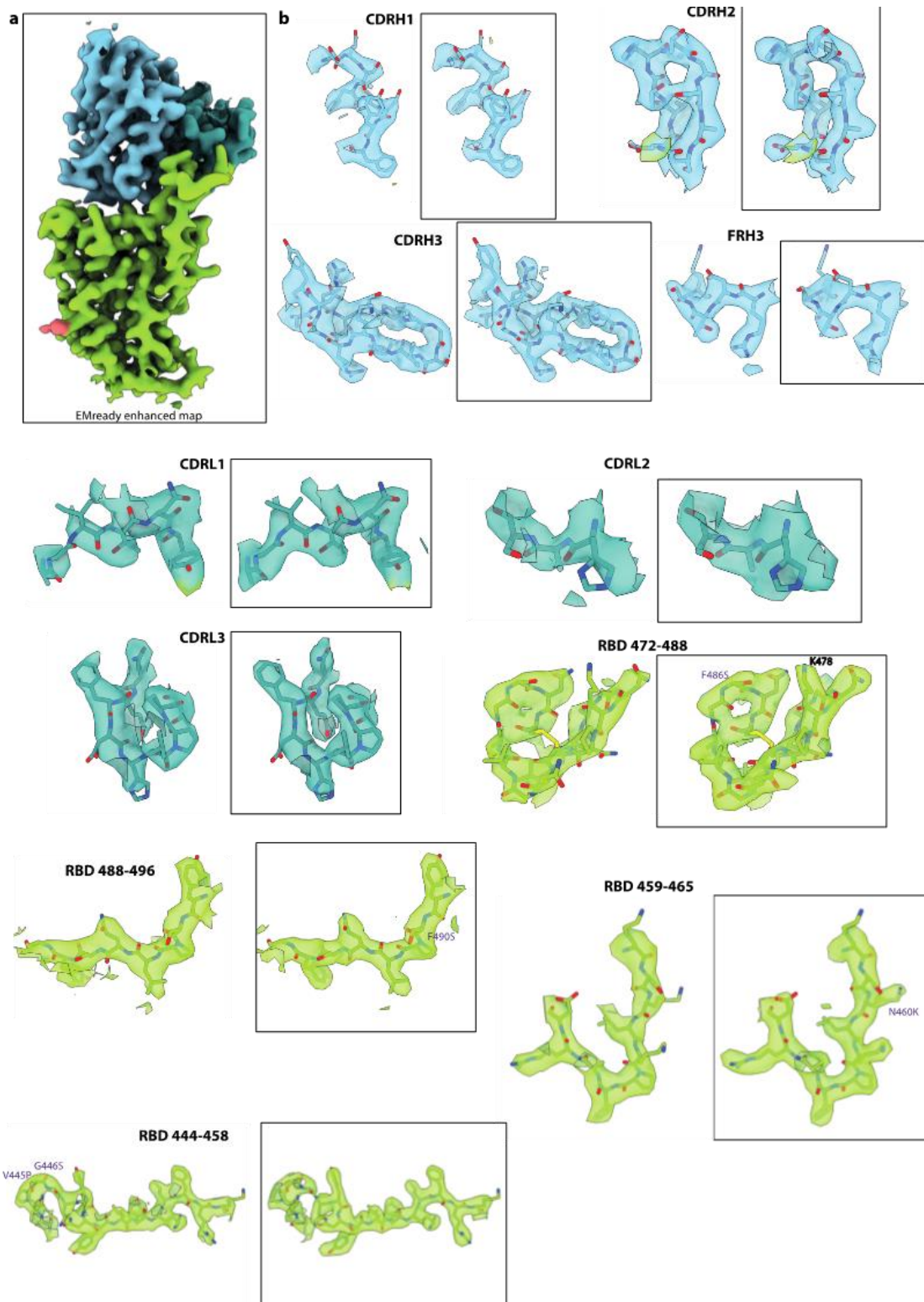
942 Competitive binding studies between antibodies binding to the 2019-nCoV Spike trimer
 943 protein. Spike coupled beads pre-incubated with saturating concentrations of competitor
 944 antibody were used for binding studies with the indicated biotinylated antibodies. Competitors
 945 induced either strong blocking (Red boxes), partial competition (orange boxes) or non-
 946 competitive (white boxes) binding with the corresponding antibody to Spike.



947

948 **Supplementary Figure 4- Details of Cryo-EM processing and Resolution maps**

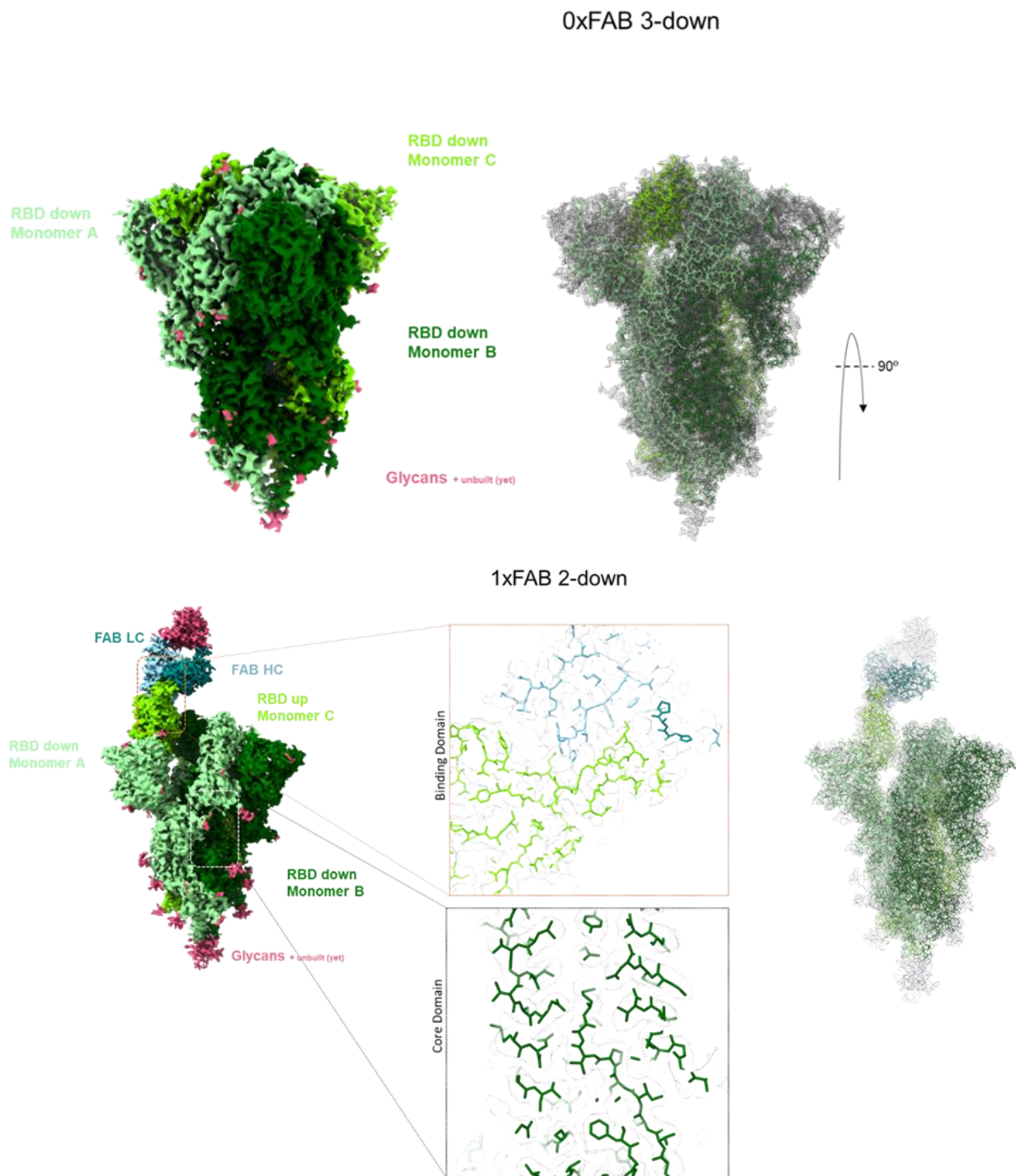
949 **a)** Raw representative micrograph. **b)** Representative 2D class averages. **c)** Cryo-EM
 950 processing workflow performed in CryoSPARC **d)** FSC curves indicating a resolution of 3.01
 951 Å of the full-length Omicron XBB.1 Spike bound to the P4J15 Fab and 3.85 Å for the focused
 952 local refinement, **e)** Direction distribution plot



953

954 **Supplementary Figure 5 - Highlights of regions of the XBB.1 RBD and P4J15 with**
 955 **Cryo-EM density maps from Cryosparc and from EMReady.**

956 The Cryo-EM density is rendered as a mesh. The atomic model is shown as ribbon or stick
 957 representation. Representations in a box are maps from EMReady.



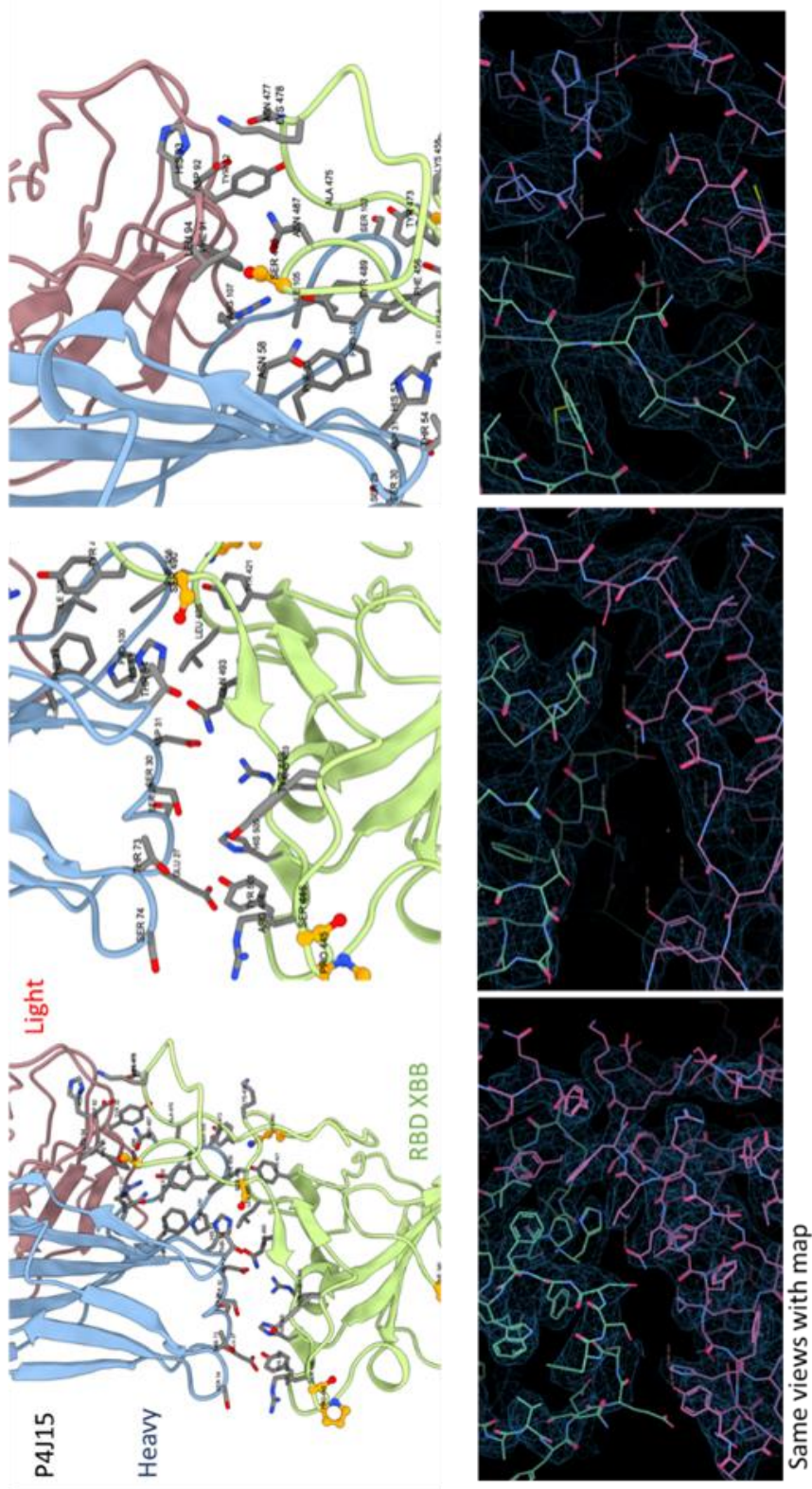
959

960 **Supplementary Figure 6- Details of Spike XBB.1 trimer 3D classifications.**

961 **a)** Spike trimer with all three RBDs in the down conformation at 2.91 Å resolution and **b)**
 962 Spike trimer with P4J15 Fab bound in the RBD up conformation and the remaining two RBD
 963 monomers in the down conformation.

964

965

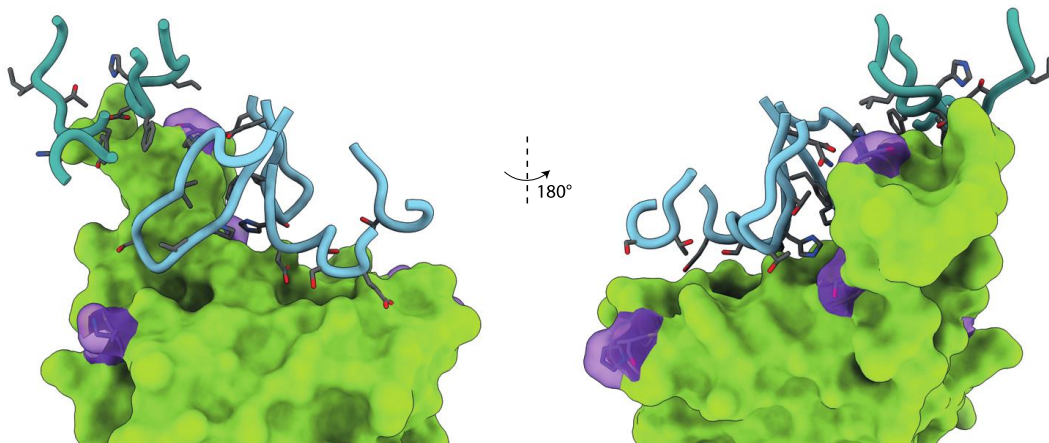


966

967 **Supplementary Figure 7- Additional views of the P4J15 Fab-Omicron XBB.1 RBD**
 968 **interactions.**

969 Ribbon structure with stick representation of contact residues for P4J15 and RBD from three
 970 different views (top panels) with corresponding mesh representation of Cryo-EM density
 971 (bottom panels).

972



973

974 **Supplementary Figure 8- Back and front view representation of the RBD (green) and**
975 **P4J15 heavy and light chain contact loops shown in cyan and turquoise**

976

977

978

979

980

981

982

983

984

985

986

987

988

989

990

991

992

993

994

995 **Supplementary Table 1: Estimated new hospitalization rates in the United States and Europe**

Country / Region	Average weekly new hospitalizations: May 1 st to June 18 th , 2023, from Our World in Data	Population	New hospitalizations per week per 100000 individuals
Belgium	248	11'590'000	2,14
Czechia	81	10'709'000	0,76
Denmark	210	5'792'000	3,62
England	2133	55'977'000	3,81
Estonia	41	1'327'000	3,08
Germany	1330	83'784'000	1,59
Greece	500	10'423'000	4,80
Hungary	36	9'660'000	0,37
Ireland	207	4'938'000	4,20
Italy	777	60'462'000	1,29
Latvia	74	1'886'000	3,92
Northern Ireland	36	1'903'000	1,87
Slovakia	44	5'460'000	0,81
Spain	1867	46'755'000	3,99
Wales	4	3'210'000	0,13
Data available for Europe countries	7587	313'875'196	2,42
United States	8028	336'862'000	2,38
Weekly new hospitalizations from Northern America and Europe	15615		

996 <https://github.com/owid/covid-19-data/tree/master/public/data/hospitalizations>

997

998

999

1000

1001

1002

1003

1004

1005

1006

1007

1008

1009

1010

1011 **Supplementary Table 2: SARS-CoV-2 Spike variant substitutions**

D614G	D614G
Alpha B.1.1.7	Δ69-70, Δ144, N501Y, A570D, D614G, P681H, T716I, S982A, D1118H
Beta B.1.351	L18F, D80A, D215G, Δ242-244, R246I, K417N, E484K, N501Y, D614G, A701V
Gamma P.1	L18F, T20N, P26S, D138Y, R190S, K417T, E484K, N501Y, D614G, H655Y, T1027I, V1176F
delta B.1.617.2	T19R, Δ156-157, R158G, L452R, T478K, D614G, P681R, D950N
delta AY.4.2	T19R, T95I, Y145H, Δ156-157, R158G, A222V, L452R, T478K, D614G, P681R, D950N
Kappa B.1.617.1	E154K, L452R, E484Q, D614G, P681R, Q1071H
Lambda C.37	G75V, T76I, R246N, del247-253, L452Q, F490S, D614G, T859N
Iota B.1.526	L5F, T95I, D253G, E484K, D614G, A701V
Eta B.1.525	Q52R, del69-70, E484K, Q677H, F888L
Omicron BA.1	A67V, Δ69-70, T95I, G142D, Δ143-145, Δ211, L212I, ins214EPE, G339D, S371L, S373P, S375F, K417N, N440K, G446S, S477N, T478K, E484A, Q493R, G496S, Q498R, N501Y, Y505H, T547K, D614G, H655Y, N679K, P681H, N764K, D796Y, N856K, Q954H, N969K, L981F
Omicron BA.1.1	A67V, Δ69-70, T95I, G142D, Δ143-145, Δ211, L212I, ins214EPE, G339D, R346K, S371L, S373P, S375F, K417N, N440K, G446S, S477N, T478K, E484A, Q493R, G496S, Q498R, N501Y, Y505H, T547K, D614G, H655Y, N679K, P681H, N764K, D796Y, N856K, Q954H, N969K, L981F
Omicron BA.2	T19I, Δ24-26, A27S, G142D, V213G, G339D, S371F, S373P, S375F, T376A, D405N, R408S, K417N, N440K, S477N, T478K, E484A, Q493R, Q498R, N501Y, Y505H, D614G, H655Y, N679K, P681H, N764K, D796Y, Q954H, N969K
Omicron BA.2.12	T19I, Δ24-26, A27S, G142D, V213G G339D, S371F, S373P, S375F, T376A, D405N, R408S, K417N, N440K, S477N, T478K, E484A, Q493R, Q498R, N501Y, Y505H, D614G, H655Y, N679K, P681H, S704L, N764K, D796Y, Q954H, N969K
Omicron BA.2.12.1	T19I, Δ24-26, A27S, G142D, V213G G339D, S371F, S373P, S375F, T376A, D405N, R408S, K417N, N440K, L452Q, S477N, T478K, E484A, Q493R, Q498R, N501Y, Y505H, D614G, H655Y, N679K, P681H, S704L, N764K, D796Y, Q954H, N969K
Omicron BA.2.75	T19I, Δ24-26, A27S, G142D, K417E, W152R, F157L, I210V, V213G, G257S, G339D, S371F, S373P, S375F, T376A, D405N, R408S, K417N, N440K, G446S, N460K, S477N, T478K, E484A, Q498R, N501Y, Y505H, D614G, H655Y, N679K, P681H, N764K, D796Y, Q954H, N969K

Omicron BA.2.75.7	T19I, Δ24-26, A27S, G142D, K417E, W152R, F157L, I210V, V213G, G257S, G339D, S371F, S373P, S375F, T376A, D405N, R408S, K417N, N440K, G446S, N460K, S477N, T478K, E484A, F486S, Q498R, N501Y, Y505H, D614G, H655Y, N679K, P681H, N764K, D796Y, Q954H, N969K
Omicron BA.2.75.2	T19I, Δ24-26, A27S, G142D, K417E, W152R, F157L, G181V, I210V, V213G, G257S, G339D, R346T, S371F, S373P, S375F, T376A, D405N, R408S, K417N, N440K, G446S, N460K, S477N, T478K, E484A, F486S, Q498R, N501Y, Y505H, D614G, H655Y, N679K, P681H, N764K, D796Y, Q954H, N969K, D1199N
Omicron BA.4 and BA.5	T19I, Δ24-26, A27S, Δ69-70, G142D, V213G, G339D, S371F, S373P, S375F, T376A, D405N, R408S, K417N, N440K, L452R, S477N, T478K, E484A, F486V, Q498R, N501Y, Y505H, D614G, H655Y, N679K, P681H, N764K, D796Y, Q954H, N969K
Omicron BF.7	T19I, Δ24-26, A27S, Δ69-70, G142D, V213G, G339D, R346T, S371F, S373P, S375F, T376A, D405N, R408S, K417N, N440K, L452R, S477N, T478K, E484A, F486V, Q498R, N501Y, Y505H, D614G, H655Y, N679K, P681H, N764K, D796Y, Q954H, N969K
Omicron BQ.1	T19I, Δ24-26, A27S, Δ69-70, G142D, V213G, G339D, S371F, S373P, S375F, T376A, D405N, R408S, K417N, N440K, K444T, L452R, N460K, S477N, T478K, E484A, F486V, Q498R, N501Y, Y505H, D614G, H655Y, N679K, P681H, N764K, D796Y, Q954H, N969K
Omicron BQ.1.1	T19I, Δ24-26, A27S, Δ69-70, G142D, V213G, G339D, R346T, S371F, S373P, S375F, T376A, D405N, R408S, K417N, N440K, K444T, L452R, N460K, S477N, T478K, E484A, F486V, Q498R, N501Y, Y505H, D614G, H655Y, N679K, P681H, N764K, D796Y, Q954H, N969K
Omicron XBB.1/XBB.1.9	T19I, Δ24-26, A27S, V83A, G142D, ΔY144, H146Q, Q183E, V213E, G252V, G339H, R346T, L368I, S371F, S373P, S375F, T376A, D405N, R408S, K417N, N440K, V445P, G446S, N460K, S477N, T478K, E484A, F486S, F490S, Q498R, N501Y, Y505H, D614G, H655Y, N679K, P681H, N764K, D796Y, Q954H, N969K
Omicron XBB.1.5/ XBB.1.9.1	T19I, Δ24-26, A27S, V83A, G142D, ΔY144, H146Q, Q183E, V213E, G252V, G339H, R346T, L368I, S371F, S373P, S375F, T376A, D405N, R408S, K417N, N440K, V445P, G446S, N460K, S477N, T478K, E484A, F486P, F490S, Q498R, N501Y, Y505H, D614G, H655Y, N679K, P681H, N764K, D796Y, Q954H, N969K
Omicron XBB.1.16	T19I, Δ24-26, A27S, V83A, G142D, ΔY144, H146Q, E180V, Q183E, V213E, G252V, G339H, R346T, L368I, S371F, S373P, S375F, T376A, D405N, R408S, K417N, N440K, V445P, G446S, N460K, S477N, T478R, E484A, F486P, F490S, Q498R, N501Y, Y505H, D614G, H655Y, N679K, P681H, N764K, D796Y, Q954H, N969K
Omicron XBB.1.16.1	T19I, Δ24-26, A27S, V83A, G142D, ΔY144, H146Q, E180V, Q183E, V213E, G252V, G339H, R346T, L368I, S371F, S373P, S375F, T376A, D405N, R408S, K417N, N440K, V445P, G446S, N460K, S477N, T478R, E484A, F486P, F490S, Q498R, N501Y, Y505H, T547I, D614G, H655Y, N679K, P681H, N764K, D796Y, Q954H, N969K
Omicron XBB.2.3	T19I, Δ24-26, A27S, V83A, G142D, ΔY144, H146Q, E180V, Q183E, V213E, D253G, G339H, R346T, L368I, S371F, S373P, S375F, T376A, D405N, R408S, K417N, N440K, V445P, G446S, N460K, S477N, T478R, E484A, F486P, F490S, Q498R, N501Y, Y505H, P521S, T547I, D614G, H655Y, N679K, P681H, N764K, D796Y, Q954H, N969K
Omicron EG.1	T19I, Δ24-26, A27S, V83A, G142D, ΔY144, H146Q, E180V, Q183E, V213E, G252V, G339H, R346T, L368I, S371F, S373P, S375F, T376A, D405N, R408S, K417N, N440K, V445P, G446S, N460K, S477N, T478R, E484A, F486P, F490S, Q498R, N501Y, Y505H, T547I, Q613H, D614G, H655Y, N679K, P681H, N764K, D796Y, Q954H, N969K

1012

1013

1014 **Supplementary Table 3: Cryo-EM data collection and refinement statistics of SPIKE-FAB**
 1015 **complex and SPIKE alone**

	XBB - P4J15 (Closed)	XBB - P4J15 (Focus)	XBB - P4J15 FULL MAP
Data collection processing	Awaiting AUTH	Awaiting AUTH	Awaiting AUTH
EMDB ID	17850	17819	Awaiting AUTH
PDB ID	8PSD	8PQ2	-
Detector	Falcon IV	Falcon IV	Falcon IV
Magnification	96 000	96 000	96 000
Voltage (kV)	300	300	300
Electron exposure (e-/A2)	50	50	50
Defocus range (um)	-0,25	-0,25	-0,25
Pixel size (A)	0,83	0,83	0,83
Symmetry imposed	C1	C1	C1
Initial particle images (no.)	6 769 807	6 769 807	6 769 807
Final particle images (no.)	65 015	95 910	95 910
Map resolution (A)	2,91	3,85	3,01
FSC threshold	0,143	0,143	0,143
Extraction box size (A)	457	457	457
Fourrier crop to box size (A)	299	299	299
Map pixel size (A)	1,268	1,268	1,268
Refinement			
Initial models used (PDB codes)	7q07	7q07	-
Model resolution (A)	2,9	3,7	-
FSC threshold	0,143	0,143	-
Map sharpening B factors (A2)	51,4	70,7	-
Model composition			
Non-hydrogen atoms	48535	5969	-
Protein residues	3076	390	-
Nucleotides	0	0	-
Ligands	36	1	-
B factors (A2)			
Protein *	74,67	69,96	-
DNA *	-	-	-
R.m.s. deviation			
Bond lenghts (A)	0,003	0,002	-
Bond angles (A)	0,47	0,501	-
Validation			
MolProbrity score	1,44	2,13	-
Clashscore	2,2	5,53	-
Poor rotamers (%)	1,6	2,73	-
<i>Ramachandran plot</i>			
Favored (%)	95,76	91,67	-
Allowed (%)	4,24	8,33	-
Disallowed (%)	0	0	-
<i>Model-to-data fit</i>			
Ccmask	0,81	0,79	-
Ccbox	0,64	0,6	-
Ccpeaks	0,6	0,44	-
CCvolume	0,79	0,66	-

1016

1017

1018 **References**

- 1019 1. WHO, E. 75, Ed. (2022), vol. July 12th, 2020.
- 1020 2. Q. Wang *et al.*, Alarming antibody evasion properties of rising SARS-CoV-2 BQ and XBB
- 1021 subvariants. *Cell* **186**, 279-286 e278 (2023).
- 1022 3. A. Akerman *et al.*, Emergence and antibody evasion of BQ, BA.2.75 and SARS-CoV-2
- 1023 recombinant sub-lineages in the face of maturing antibody breadth at the population level.
- 1024 *EBioMedicine* **90**, 104545 (2023).
- 1025 4. K. Uriu *et al.*, Enhanced transmissibility, infectivity, and immune resistance of the SARS-CoV-2
- 1026 omicron XBB.1.5 variant. *Lancet Infect Dis* **23**, 280-281 (2023).
- 1027 5. P. Qu *et al.*, Enhanced evasion of neutralizing antibody response by Omicron XBB.1.5, CH.1.1,
- 1028 and CA.3.1 variants. *Cell Rep* **42**, 112443 (2023).
- 1029 6. S. Flaxman *et al.*, Assessment of COVID-19 as the Underlying Cause of Death Among Children
- 1030 and Young People Aged 0 to 19 Years in the US. *JAMA Netw Open* **6**, e2253590 (2023).
- 1031 7. A. Casadevall, D. Focosi, SARS-CoV-2 variants resistant to monoclonal antibodies in
- 1032 immunocompromised patients constitute a public health concern. *J Clin Invest* **133**, (2023).
- 1033 8. M. Patel *et al.*, Analysis of MarketScan Data for Immunosuppressive Conditions and
- 1034 Hospitalizations for Acute Respiratory Illness, United States. *Emerg Infect Dis* **26**, 1720-1730
- 1035 (2020).
- 1036 9. S. Mbaeyi *et al.*, The Advisory Committee on Immunization Practices' Interim
- 1037 Recommendations for Additional Primary and Booster Doses of COVID-19 Vaccines - United
- 1038 States, 2021. *MMWR Morb Mortal Wkly Rep* **70**, 1545-1552 (2021).
- 1039 10. J. D. Kelly *et al.*, Incidence of Severe COVID-19 Illness Following Vaccination and Booster With
- 1040 BNT162b2, mRNA-1273, and Ad26.COVS.2 Vaccines. *JAMA* **328**, 1427-1437 (2022).
- 1041 11. Y. Cao *et al.*, Imprinted SARS-CoV-2 humoral immunity induces convergent Omicron RBD
- 1042 evolution. *Nature* **614**, 521-529 (2023).
- 1043 12. Y. Feng *et al.*, Broadly neutralizing antibodies against sarbecoviruses generated by
- 1044 immunization of macaques with an AS03-adjuvanted COVID-19 vaccine. *Sci Transl Med* **15**,
- 1045 eadg7404 (2023).
- 1046 13. L. Liu *et al.*, Antibodies that neutralize all current SARS-CoV-2 variants of concern by
- 1047 conformational locking. *bioRxiv*, (2023).
- 1048 14. J. Guenthoer *et al.*, Identification of broad, potent antibodies to functionally constrained
- 1049 regions of SARS-CoV-2 spike following a breakthrough infection. *Proc Natl Acad Sci U S A* **120**,
- 1050 e2220948120 (2023).
- 1051 15. P. Zhou *et al.*, Broadly neutralizing anti-S2 antibodies protect against all three human
- 1052 betacoronaviruses that cause deadly disease. *Immunity* **56**, 669-686 e667 (2023).
- 1053 16. C. Fenwick *et al.*, A high-throughput cell- and virus-free assay shows reduced neutralization
- 1054 of SARS-CoV-2 variants by COVID-19 convalescent plasma. *Sci Transl Med* **13**, (2021).
- 1055 17. J. Dong *et al.*, Genetic and structural basis for SARS-CoV-2 variant neutralization by a two-
- 1056 antibody cocktail. *Nat Microbiol* **6**, 1233-1244 (2021).
- 1057 18. C. G. Rappazzo *et al.*, An Engineered Antibody with Broad Protective Efficacy in Murine
- 1058 Models of SARS and COVID-19. *bioRxiv*, (2020).
- 1059 19. K. Westendorf *et al.*, LY-CoV1404 (bebtelovimab) potently neutralizes SARS-CoV-2 variants.
- 1060 *Cell Rep* **39**, 110812 (2022).
- 1061 20. D. Pinto *et al.*, Cross-neutralization of SARS-CoV-2 by a human monoclonal SARS-CoV
- 1062 antibody. *Nature* **583**, 290-295 (2020).
- 1063 21. C. Fenwick *et al.*, A highly potent antibody effective against SARS-CoV-2 variants of concern.
- 1064 *Cell Rep* **37**, 109814 (2021).
- 1065 22. C. Fenwick *et al.*, Patient-derived monoclonal antibody neutralizes SARS-CoV-2 Omicron
- 1066 variants and confers full protection in monkeys. *Nat Microbiol* **7**, 1376-1389 (2022).
- 1067 23. J. He, T. Li, S. Y. Huang, Improvement of cryo-EM maps by simultaneous local and non-local
- 1068 deep learning. *Nat Commun* **14**, 3217 (2023).

- 1069 24. T. N. Starr *et al.*, Deep mutational scans for ACE2 binding, RBD expression, and antibody
1070 escape in the SARS-CoV-2 Omicron BA.1 and BA.2 receptor-binding domains. *PLoS Pathog* **18**,
1071 e1010951 (2022).
- 1072 25. Y. M. Loo *et al.*, The SARS-CoV-2 monoclonal antibody combination, AZD7442, is protective in
1073 nonhuman primates and has an extended half-life in humans. *Sci Transl Med* **14**, eabl8124
1074 (2022).
- 1075 26. T. Thaweethai *et al.*, Development of a Definition of Postacute Sequelae of SARS-CoV-2
1076 Infection. *JAMA* **329**, 1934-1946 (2023).
- 1077 27. J. Ito *et al.*, Convergent evolution of SARS-CoV-2 Omicron subvariants leading to the
1078 emergence of BQ.1.1 variant. *Nat Commun* **14**, 2671 (2023).
- 1079 28. T. Tamura *et al.*, Virological characteristics of the SARS-CoV-2 XBB variant derived from
1080 recombination of two Omicron subvariants. *Nat Commun* **14**, 2800 (2023).
- 1081 29. L. Witte *et al.*, Epistasis lowers the genetic barrier to SARS-CoV-2 neutralizing antibody
1082 escape. *Nat Commun* **14**, 302 (2023).
- 1083 30. B. E. Jones *et al.*, The neutralizing antibody, LY-CoV555, protects against SARS-CoV-2
1084 infection in nonhuman primates. *Sci Transl Med* **13**, (2021).
- 1085 31. M. Hashimoto *et al.*, Immunogenicity and protective efficacy of SARS-CoV-2 recombinant S-
1086 protein vaccine S-268019-b in cynomolgus monkeys. *Vaccine* **40**, 4231-4241 (2022).
- 1087 32. J. Zalevsky *et al.*, Enhanced antibody half-life improves in vivo activity. *Nat Biotechnol* **28**,
1088 157-159 (2010).
- 1089 33. A. H. Mohammed, A. Blebil, J. Dujaili, B. A. Rasool-Hassan, The Risk and Impact of COVID-19
1090 Pandemic on Immunosuppressed Patients: Cancer, HIV, and Solid Organ Transplant
1091 Recipients. *AIDS Rev* **22**, 151-157 (2020).
- 1092 34. M. Ragonnet-Cronin *et al.*, Generation of SARS-CoV-2 escape mutations by monoclonal
1093 antibody therapy. *Nat Commun* **14**, 3334 (2023).
- 1094 35. M. Obeid *et al.*, Humoral Responses Against Variants of Concern by COVID-19 mRNA
1095 Vaccines in Immunocompromised Patients. *JAMA Oncol*, (2022).
- 1096 36. D. Wrapp *et al.*, Cryo-EM structure of the 2019-nCoV spike in the prefusion conformation.
1097 *Science* **367**, 1260-1263 (2020).
- 1098 37. C. Fenwick *et al.*, Changes in SARS-CoV-2 Spike versus Nucleoprotein Antibody Responses
1099 Impact the Estimates of Infections in Population-Based Seroprevalence Studies. *J Virol* **95**,
1100 (2021).
- 1101 38. A. M. Syed *et al.*, Rapid assessment of SARS-CoV-2-evolved variants using virus-like particles.
1102 *Science* **374**, 1626-1632 (2021).
- 1103 39. P. Maisonnasse *et al.*, COVA1-18 neutralizing antibody protects against SARS-CoV-2 in three
1104 preclinical models. *Nat Commun* **12**, 6097 (2021).
- 1105 40. P. Maisonnasse *et al.*, Hydroxychloroquine use against SARS-CoV-2 infection in non-human
1106 primates. *Nature* **585**, 584-587 (2020).
- 1107 41. R. Boudewijns *et al.*, STAT2 signaling restricts viral dissemination but drives severe
1108 pneumonia in SARS-CoV-2 infected hamsters. *Nat Commun* **11**, 5838 (2020).
- 1109 42. S. J. F. Kaptein *et al.*, Favipiravir at high doses has potent antiviral activity in SARS-CoV-2-
1110 infected hamsters, whereas hydroxychloroquine lacks activity. *Proc Natl Acad Sci U S A* **117**,
1111 26955-26965 (2020).
- 1112 43. L. Sanchez-Felipe *et al.*, A single-dose live-attenuated YF17D-vectored SARS-CoV-2 vaccine
1113 candidate. *Nature* **590**, 320-325 (2021).
- 1114 44. A. Punjani, J. L. Rubinstein, D. J. Fleet, M. A. Brubaker, cryoSPARC: algorithms for rapid
1115 unsupervised cryo-EM structure determination. *Nat Methods* **14**, 290-296 (2017).
- 1116 45. J. L. Rubinstein, M. A. Brubaker, Alignment of cryo-EM movies of individual particles by
1117 optimization of image translations. *J Struct Biol* **192**, 188-195 (2015).
- 1118 46. E. F. Pettersen *et al.*, UCSF ChimeraX: Structure visualization for researchers, educators, and
1119 developers. *Protein Sci* **30**, 70-82 (2021).

- 1120 47. K. Jamali *et al.*, Automated model building and protein identification in cryo-EM maps.
1121 *bioRxiv*, (2023).
- 1122 48. P. Emsley, B. Lohkamp, W. G. Scott, K. Cowtan, Features and development of Coot. *Acta*
1123 *Crystallogr D Biol Crystallogr* **66**, 486-501 (2010).
- 1124 49. D. Liebschner *et al.*, Macromolecular structure determination using X-rays, neutrons and
1125 electrons: recent developments in Phenix. *Acta Crystallogr D Struct Biol* **75**, 861-877 (2019).
- 1126